Live imaging of reporter zebrafish reveals dynamics and molecular basis of physiological-stress induced mitophagy.

Paul J. Wrighton[1], Arkadi Shwartz[1], Jin-Mi Heo[2], Eleanor D. Quenzer[1], Kyle A. LaBella[1], J. Wade Harper[2], Wolfram Goessling[1,3,4,5,6,7,8,*]

[1]Division of Genetics, Brigham and Women's Hospital, Harvard Medical School, Boston, MA 02115, USA.

[2]Department of Cell Biology, Harvard Medical School, Boston, MA 02115, USA.

[3]Harvard Stem Cell Institute, Cambridge, MA 02138, USA.

[4]Dana-Farber Cancer Institute, Harvard Medical School, Boston, MA 02115, USA.

[5]Broad Institute of MIT and Harvard, Cambridge, MA 02142, USA.

[6]Harvard-MIT Division of Health Sciences and Technology, Boston, MA 02115, USA.

[7]Division of Gastroenterology, Massachusetts General Hospital, Harvard Medical School, Boston, MA 02114, USA.

[8]Lead Contact

*Correspondence: wgoessling@mgh.harvard.edu

ABSTRACT

Defects in mitophagy, the selective recycling of mitochondria through autophagy, are linked to aging, sarcopenia, and neurodegenerative diseases. To therapeutically target mitophagy, the dynamics and molecular mechanisms *in vivo* must be understood. Here, we describe newly generated mitophagy biosensor zebrafish, reveal widespread basal mitophagy during normal development, and illuminate the dynamics and molecular mechanisms of mitophagy induced by physiological stresses—fasting and hypoxia. In fasted muscle, volumetric quantification of mitolysosome size uncovered organelle stress-response dynamics, and live, time-lapse imaging revealed mitophagy occurred via a piecemeal rather than wholesale process. Activating Hypoxia-inducible factor through physiological hypoxia or chemical or genetic modulation also provoked mitophagy. Surprisingly, disruption of a single mitophagy receptor *bnip3* mitigated the response. Disruption of *bnip3la* (*nix*) or *fundc1*, putative hypoxia-associated mitophagy receptors, or *pink1* or *prkn* (Parkin) had no effect. This *in vivo* imaging study establishes fundamental dynamics of fasting-induced mitophagy and elucidates molecular mechanisms governing hypoxia-induced mitophagy.

KEYWORDS

Autophagy, Hypoxia, Fasting, Mitochondria, Lysosome

Mitophagy, the removal of damaged mitochondria via autophagy, prevents cellular damage and apoptosis (Youle, 2019). Defective mitophagy has been linked to muscular dysfunction (Sandri, 2013), neurodegenerative diseases (Pickrell and Youle, 2015), and drug-induced liver injury (Wrighton et al., 2019). Recently, mitophagy has also been found to occur at a basal level in most cells, especially those with high metabolic rates (McWilliams et al., 2018, 2016; Sun et al., 2015). However, the extent of basal mitophagy is unclear, especially during embryonic development. Further, the fundamental organelle dynamics and associated molecular mechanisms of stress-induced mitophagy have been investigated primarily using *in vitro* cell culture systems. *In vivo* studies may provide novel mechanistic insight that could enable effective targeting of mitophagy for therapeutic purposes.

The organelle dynamics and interactions between mitochondria, autophagosomes, autolysosomes, and lysosomes in response to physiological stresses are underexplored *in vivo*. Fasting induces lysosome biogenesis and autophagy (Preidis et al., 2017; Raefsky and Mattson, 2017; Sebastián and Zorzano, 2020; Settembre et al., 2013), but how mitolysosome (lysosomes containing mitochondria for degradation) size or number changes in response to increasing mitophagic demand are unknown. Additionally, there are multiple mechanisms proposed in cells cultured *in vitro* by which a mitochondrion is sequestered by the autophagy machinery. In the "wholesale" mode, after a mitochondrial filament reaches a damage threshold, mitochondrial membrane depolarization and extensive fragmentation occurs, which is followed by recruitment of the autophagy machinery to degrade the fragments. In the "piecemeal" mode, the damaged part of a mitochondrial filament is sequestered, and the autophagy machinery is localized to that point, which undergoes fission and degradation, leaving the filament largely intact (Burman et al., 2017; Yamashita et al., 2016; Youle, 2019). These mitophagy modes have not been verified in any live organism or stress context, highlighting the need for live imaging, *in vivo* interrogation.

Most molecular mechanisms governing mitophagy were initially described in cell lines overexpressing the mitophagy activator PARKIN and non-physiological stresses, such as exposure to mitochondrial uncouplers. Hypoxia is a physiological stress that induces mitophagy in cultured mouse embryonic fibroblasts (MEFs) (Zhang et al., 2008) as well as murine liver (Sun et al., 2015) and muscle (Zhang et al., 2008). The mechanisms governing hypoxia-induced mitophagy remain to be fully elucidated. While Bnip3-Fox03 signaling is linked to fasting-induced macroautophagy in muscle (Mammucari et al., 2007), hypoxia-induced mitophagy has not been examined. Further, the PINK1-PARKIN pathway governs mitochondrial depolarization-induced mitophagy (Harper et al., 2018; Pickles et al., 2018), however, its role in hypoxia-induced mitophagy remains controversial with evidence in other model organisms both for (Kim et al., 2019; T. Zhang et al., 2016) and against (Lee et al., 2018) a role. Thus, genetic epistasis analyses using *in vivo* models to dissect which mitophagy receptors or pathways are active in different tissues and under different stresses will further elucidate this process.

Recently, mitochondria-targeted, pH-sensitive fluorescent protein constructs—mito-mKeima (mito-Keima) (Katayama et al., 2011) and mito-EGFP-mCherry (mito-GR; Green Red) (Rojansky et al., 2016)—have been developed as sensitive readouts of mitophagy and incorporated into cell culture models and model organisms (Lee et al., 2018; McWilliams et al., 2016; Ordureau et al., 2020; Sun et al., 2015). Keima is a fluorescent, red light-emitting protein with a pH-sensitive excitation spectrum, enabling differentiation between Keima in a slightly basic pH environment, such as the healthy mitochondrial matrix (Porcelli et al., 2005), or an acidic environment, such as an autolysosome (Katayama et al., 2011). Whereas EGFP is sensitive to acid quenching and lysosomal degradation, mCherry and Keima are resistant to lysosomal degradation, allowing for signal accumulation, which is an indicator of the extent of mitophagic flux (Katayama et al., 2008). Combining these tools with live, intravital imaging modalities offers the potential to reveal *in vivo* mitophagy dynamics and mechanisms.

Here, we generated mitophagy biosensor zebrafish and defined mitochondrial dynamics during vertebrate organ development and physiological stress. We discovered widespread basal mitophagy in many organs during development. Using time-lapse confocal fluorescence imaging, we illuminated mitophagy dynamics *in vivo*, directly observing piecemeal mitophagy in fasted muscle. We demonstrated that physiological hypoxia or chemical or genetic activation of the Hypoxia inducible factor (Hif) pathway induced mitophagy in skeletal muscle. Importantly, using precise genetic loss-of-function analyses, we demonstrated that *bnip3* is necessary for Hif-induced mitophagy in muscle independent of other reported hypoxia-associated mitophagy receptors and independent of the *pink1-prkn* (Parkin) pathway. In sum, we established fundamental *in vivo* dynamics of fasting-induced mitophagy and elucidated the genetic and molecular mechanisms governing hypoxia-induced mitophagy.

RESULTS

Biosensor zebrafish lines report *bone fide* mitophagy

Zebrafish lines *Tg(ubi:mito-Keima)* and *Tg(ubi:mito-GR)* were generated to express mito-Keima or mito-GR under the control of the ubiquitous *ubiquitin* promoter (Kwan et al., 2007; Mosimann et al., 2011). Importantly, these reporters are targeted to the mitochondrial matrix because reporters targeted to other mitochondrial locations can lead to false positive signals (Katayama et al., 2020). Healthy mitochondria maintain a pH 7.8 matrix (Porcelli et al., 2005) and can be distinguished by either a high Keima440/Keima561 ratio (Keima signal when excited by a 440 nm laser divided by Keima signal when excited by a 561 nm laser) or presence of both EGFP and mCherry. In contrast, mitochondria undergoing degradation exist in acidic autolysosomes and are distinguished by a high Keima561/Keima440 ratio for mito-Keima or presence of mCherry alone for mito-GR.

Ubi:mito-Keima and ubi:mito-GR transgenic zebrafish demonstrated no physiological abnormalities to suggest fluorophore toxicity and were generally analyzed as larvae from 1 to 8

days post fertilization (dpf). To test whether the ubi:mito-Keima construct faithfully reports mitophagy *in vivo*, we exposed ubi:mito-Keima larvae to MitoTracker Green dye, which labels all mitochondria regardless of polarization state, and found that both Keima440^{high} puncta and Keima561^{high} puncta colocalized with MitoTracker Green signal in skin cells (Figure 1A). Thus, mito-Keima is correctly localized to mitochondria even after transition to a low-pH environment. In skeletal muscle cells, LysoTracker dye, which accumulates in lysosomes, colocalized with Keima561^{high} puncta, but not with Keima440^{high} puncta (Figure 1B). Thus, areas with a high Keima561/Keima440 signal ratio represent mitolysosomes. Further, we crossed ubi:mito-Keima fish with *Tg(CMV:EGFP-Lc3)* fish, which label autophagosomes and autolysosomes with EGFP (He et al., 2009). In skeletal muscle, Keima561^{high} fluorescence colocalized with the EGFP-Lc3 signal, indicating that to induce degradation, mitochondrial fragments are shuttled to low-pH, Lc3^{+} autolysosomes (Figure 1C). Similarly, we incubated ubi:mito-GR embryos with LysoTracker deep red and observed colocalization with mCherry^{+};GFP^{-} puncta (Figure 1D). To ensure macroautophagy was necessary for the reporter signal, larvae were subjected to morpholino (MO)-mediated knockdown of the essential autophagy gene *atg5*. This induced cardiac and central nervous system defects in both ubi:mitoKeima and ubi:mito-GR embryos as previously described (Lee et al., 2016, 2014). However, notochords developed similarly at 48 hpf and displayed greatly reduced Keima561^{high} and mCherry^{+};EGFP^{-} signals (Figure 1E). Thus, both biosensor lines faithfully differentiate between healthy mitochondria and those undergoing mitophagy.

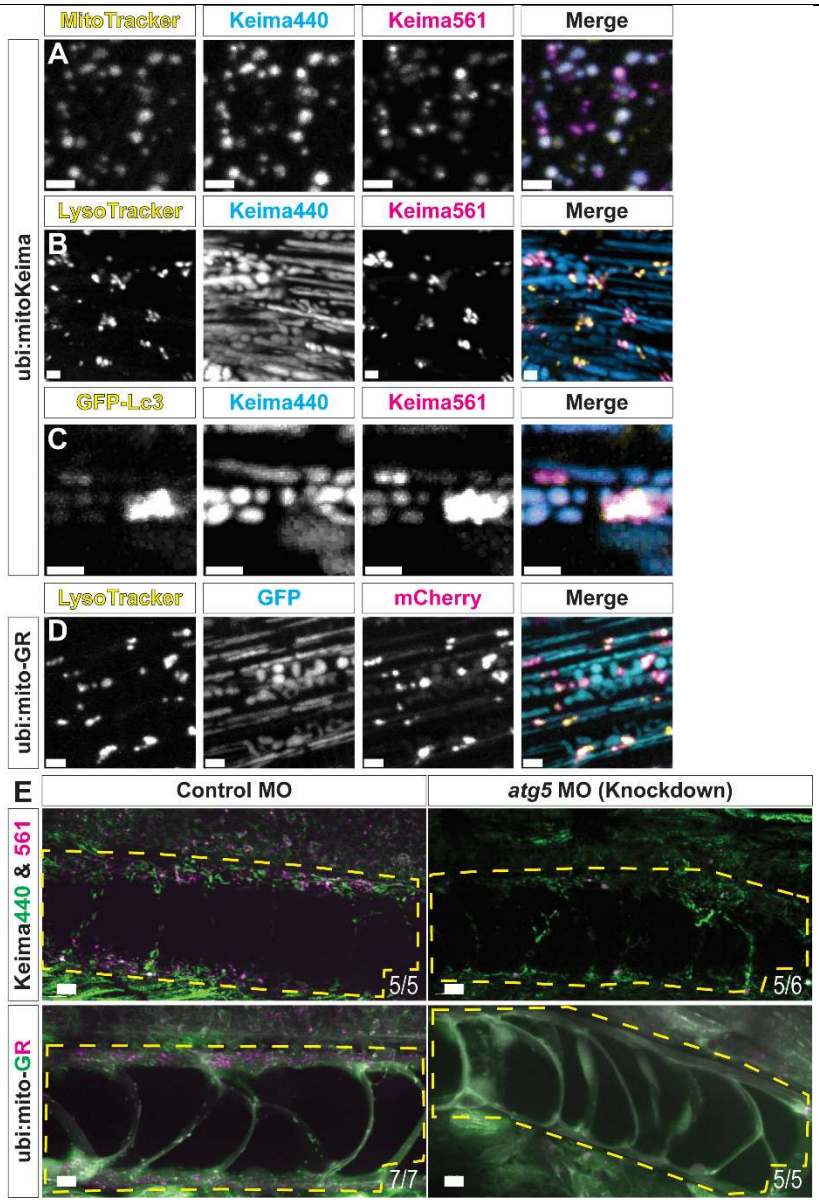

Figure 1. Reporter zebrafish faithfully differentiate healthy mitochondria and those undergoing mitophagy. (A) Maximum intensity projection (MIP) confocal images of skin cells of ubi:mito-Keima zebrafish larva treated with MitoTracker Green, showing colocalization of MitoTracker puncta with both Keima440^{high} puncta and Keima561^{high} puncta. (B) MIP confocal images of skeletal muscle cells in ubi:mito-Keima zebrafish larva treated with LysoTracker Green, showing colocalization between the Keima561^{high} puncta and LysoTracker puncta. (C) MIP confocal images of a ubi:mito-Keima;CMV:GFP-Lc3 zebrafish larva, demonstrating colocalization between Lc3^{+} puncta and Keima561^{high} puncta. (D) MIP confocal images of a ubi:mito-GR zebrafish larva treated with LysoTracker Deep Red, demonstrating colocalization between LysoTracker and the mCherry^{+};EGFP^{-} puncta. Scale bars, 3 μm. (E) MIP confocal images of 48 hpf ubi:mitoKeima and ubi:mito-GR larvae injected with control or *atg5*-targeting morpholinos. Yellow dashed boxes highlight the notochord. Control MO-injected larvae have prominent levels of mitophagy (indicated by magenta puncta), whereas *atg5* MO-injected larvae have reduced mitophagy in the notochord. The numbers in the bottom right corners indicate the proportion of larvae observed with similar phenotypes. Scale bars, 10 μm.

Transparent larvae reveal widespread mitophagy during organogenesis

While basal mitophagy has been observed in many highly metabolic adult tissues (McWilliams et al., 2016), much less is known about mitophagy during vertebrate development. We utilized the mito-GR line to delineate basal levels of mitophagy during organogenesis and observed basal mitophagy in several larval tissues, indicated by dense mCherry^{+};EGFP^{-} signal. Neural tissues including the hindbrain, olfactory placode, trigeminal ganglion, retina, spinal cord, and neuromasts had high levels of basal mitophagy. The developing notochord, vasculature, heart (ventricle), kidney, and liver all displayed high levels of basal mitophagy, and the pancreas displayed moderate levels (Figure 2A). In contrast, the onset of skeletal muscle mitophagy coincided with the stage during which zebrafish larvae must transition from subsisting on yolk sac deposited nutrients to external food sources absorbed through their gut (Wilson, 2012). Prior to 4 dpf, larval skeletal muscle exhibited minimal mitophagy, but if left without external nutrition after 5 dpf when they no longer depend on nutrients in the yolk-sac, larvae exhibited a dramatic increase in mitophagy (Figure 2B, arrows). These results reveal widespread basal mitophagy throughout development and identify zebrafish skeletal muscle as uniquely suited to investigate stress-induced mitophagy *in vivo*.

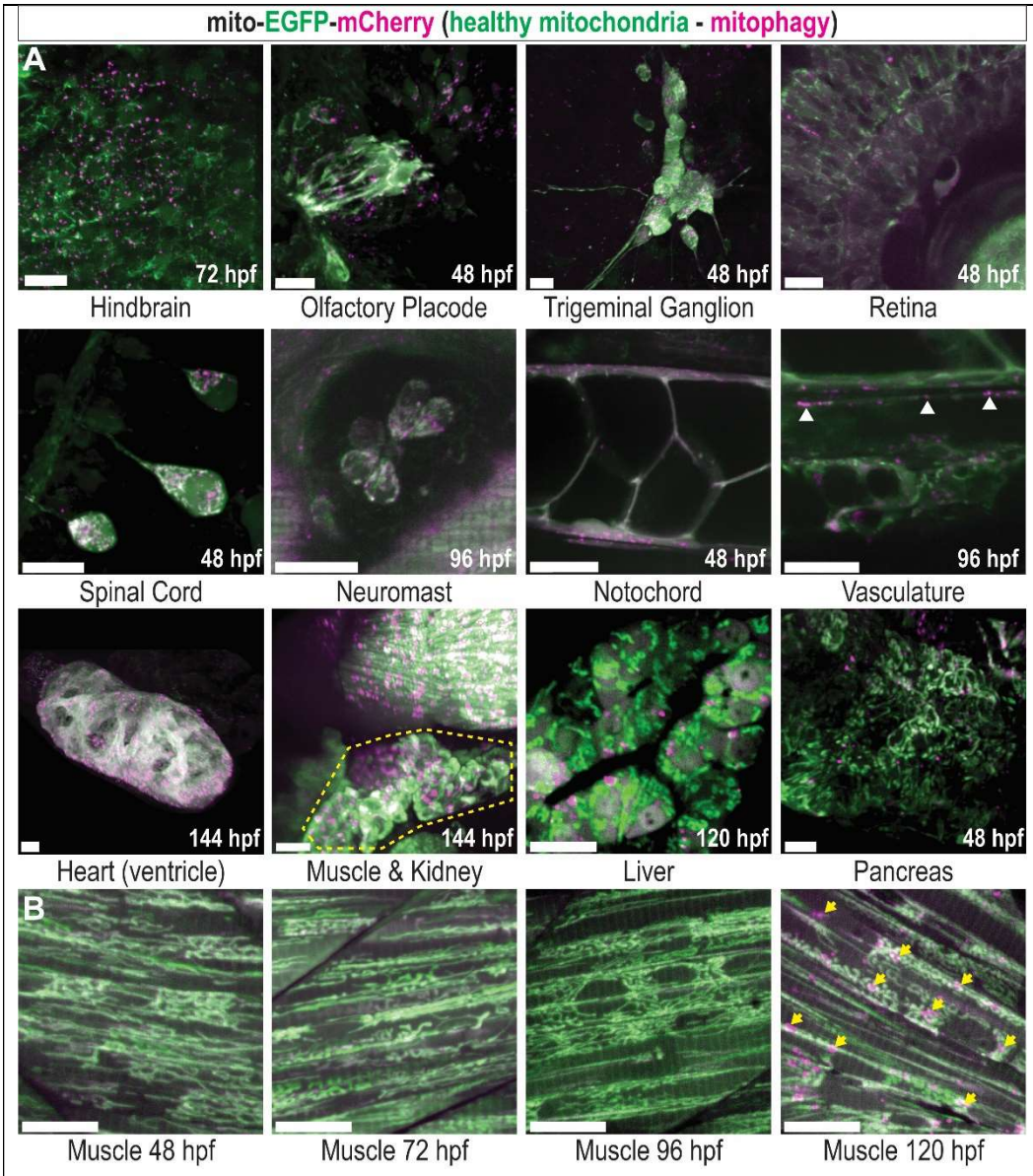

Figure 2. Basal mitophagy is widespread in developing zebrafish tissues. (A) MIP confocal images of mito-GR zebrafish larvae at the indicated developmental time points, displaying various developing organs and tissues. Green indicates EGFP^{high} mitochondria, which are healthy, and magenta indicates mCherry^{high} puncta, representing mitolysosomes (mitophagy). White arrowheads show mitophagy occurring in the vasculature. Yellow outline highlights the developing kidney. (B) Developmental time series of mito-GR skeletal muscle in the tail. Mitophagy is low at 48, 72, and 96 hpf but high at 120 hpf (arrows). All images are of live ubi:mito-GR larvae except the liver image, which is from a hepatocyte-specific fabp10a:mito-GR larva, and the heart image, which is a fixed whole-mount ubi:mito-GR larva. Scale bars, 15 μm.

Fasting induces quantifiable mitophagy and reveals mitolysosome dynamics

Skeletal muscle is a mitochondria-rich, highly metabolic tissue, which responds to nutrient deprivation by inducing autophagy (Mammucari et al., 2007), yet the regulation and dynamics of muscle mitophagy *in vivo* are not fully investigated. To precisely quantify mitophagy levels, we developed volumetric and ratiometric image acquisition and analysis methods to rapidly quantify number and size of mitolysosomes within 3D tissue volumes. Spinning disc confocal fluorescence imaging enabled rapid generation of 3D images of zebrafish muscle spanning >6 myotomes more than 150 μm deep (Figure 3A) at mitochondrial resolution (Figure 3A'; inset of Figure 3A). The Keima561/Keima440 signal ratio allows isolation of mitolysosomes (Figure 3A"), the number and volume of which can be measured through an isosurface rendering algorithm. Normalizing mitolysosome number or volume to total tissue volume yields two mitophagy quantification methods (Figure 3B and Movie 1). This process is also applicable to mito-GR, but at greater imaging depths the ubi:mito-Keima signal decayed more consistently and provided higher signal-to-noise. Thus, we applied this method to quantify fasting-induced mitophagy in ubi:mito-Keima zebrafish in two modes: mitolysosome density, defined as the number of mitolysosomes per tissue volume, and mitophagy index, defined as the proportion of total tissue volume occupied by mitolysosomes.

At 5 dpf quantifiable mitophagy was observed in both fed and fasted zebrafish muscle, but there was not a significant difference in the extent measured by mitolysosome density (Figure 3D) or mitophagy index (Figure 3E). However, mitophagy index was a more sensitive readout for mitophagy. Mitolysosome density was not significantly different between fed and fasted larvae until after 7 dpf, whereas the volumetric mitophagy index revealed increases by 6 dpf. Thus, mitophagy in skeletal muscle occurs after yolk depletion, but is abrogated by feeding.

To understand mitolysosome size dynamics, the volume distributions of individual mitolysosomes were assessed by volumetric image analysis. In fasted skeletal muscle, the early

response from 5-7 dpf was an increase in the volume distribution of mitolysosomes. Both fed and fasted fish had a monomodal mitolysosome volume distribution with the fasted fish displaying an increase in 25th , 50th, and 75th percentile mitolysosome volume (Figure 3F, and Figure 3—figure supplement 1). However, by 8 dpf, when fasting entered a more advanced stage, mitolysosome size distribution became bimodal, with an increase in both large and small mitolysosomes (Figure 3F). Surprisingly, this result is unique to mitolysosome dynamics. Although the size distribution of all LysoTracker^{+} lysosomes showed increased size and number in fasted larvae over time, very small lysosomes were present at all stages (Figure 3—figure supplement 2). Together, these results reveal that the early fasting-induced mitophagy response primarily utilizes and expands existing autolysosomes within the cell as evident by an increase in mitophagy index and shift in the size distribution prior to significant changes in the number of mitolysosomes (mitolysosome density). During advanced fasting stages, however, the existing mitolysosomes become large, and new, small mitolysosomes appear. Taken together, these data validate the volumetric mitophagy quantification method and reveal novel mitolysosome size changes as a response to prolonged nutrient deprivation.

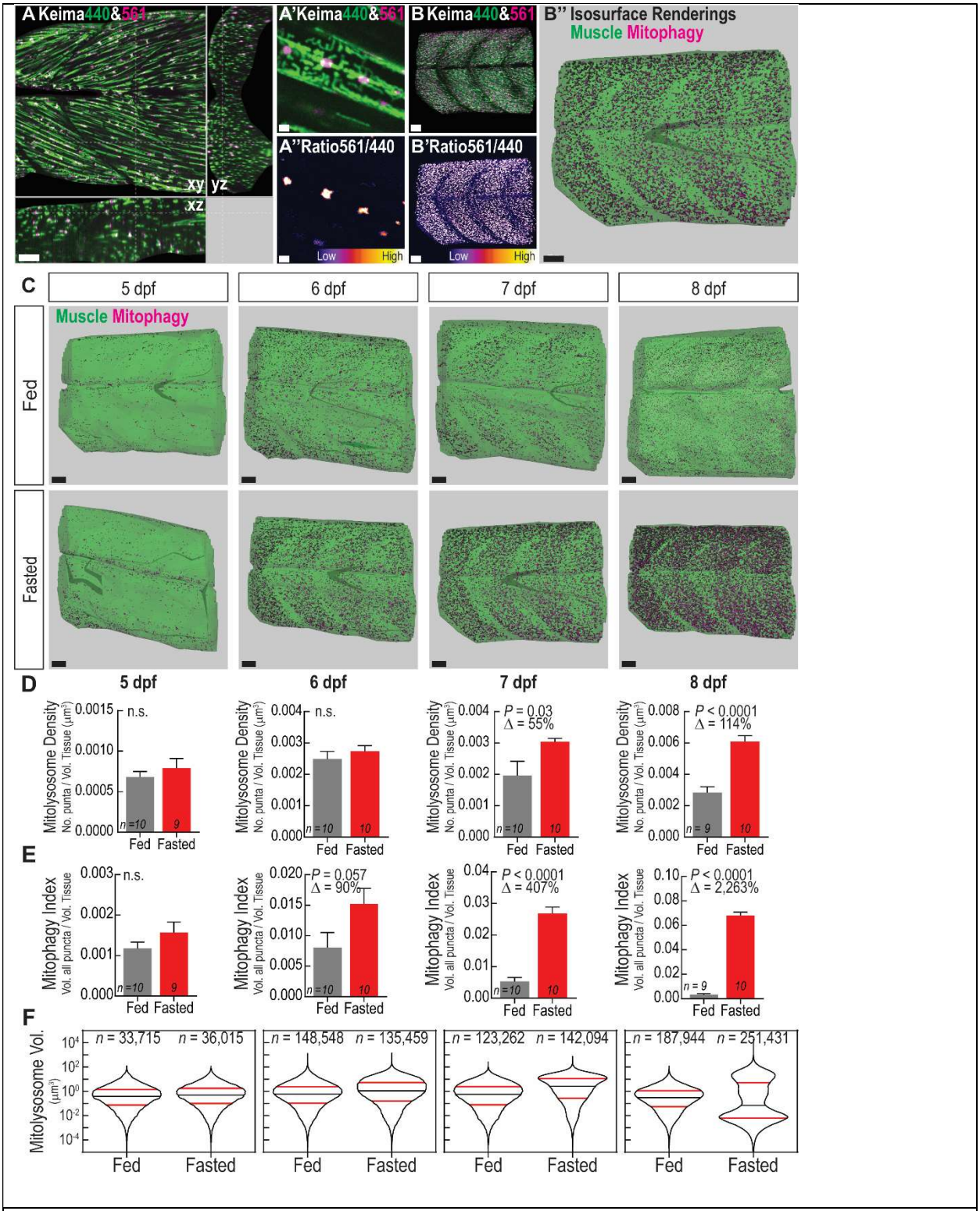

Figure 3. Fasting induces mitophagy in skeletal muscle and volumetric imaging reveals mitolysosome size dynamics. (A) Confocal microscopy cross-sectional image of 6 dpf ubi:mito-Keima zebrafish skeletal muscle demonstrates the typical imaging volume achieved for analyses. Scale, 100 μm. (A') Zoomed inset of (A) image demonstrates mitochondrial resolution achieved for all images and (A'') ratiometric images used to segment mitolysosomes. Scale, 3 μm. (B,B',B'') Representation of the image analysis process. (B) 3D reconstruction of the

large volume image showing Keima440 and Keima561 signal throughout greater than 6 myotomes. Scale, 30 μm. (B') Ratiometric image isolates Keima561^{high} mitolysosomes. Scale, 30 μm. (B'') Isosurface renderings of muscle tissue volume (green) and the mitolysosomes (magenta) allow for volumetric analysis of mitophagy. Scale, 30 μm. (C) Isosurface renderings of muscle volume and mitolysosomes in 5-8 dpf zebrafish either fed or fasted. Green is the surface rendering of the muscle tissue, and magenta are surface renderings for individual mitolysosomes. Scale, 30 μm. (D) Quantification of Mitolysosome Density defined as the number of mitolysosomes divided by the total tissue volume. (E) Quantification of Mitophagy Index defined as the sum of the volumes of all mitolysosomes divided by the total tissue volume. (D,E) Data shown are mean + SEM. *P*, unpaired, two-tailed Student's t test. n.s., not significant ($P>0.05$). Δ, percentage change of experimental cohort to control cohort. *n* indicates number of larvae in each cohort. (F) Violin plots demonstrating volume (μm^3) distribution of individual mitolysosomes from all fed or fasted zebrafish in each cohort. Significant changes in the size distributions are evident at every time point (see Figure 3—figure supplement 1). 50th percentile - black line; 25th and 75th percentiles - red lines. *n*, number of individual mitolysosomes combined from all larvae.

To determine the origin of the newly appearing small mitolysosomes found in advanced fasting stages, we performed rapid, continuous time-lapse analysis on a 7 dpf fasted mito-Keima larva (Movie 2). Application of an object tracking algorithm enabled identification of *de novo* mitophagy and mitolysosome fission events (Figure 4A). Each event was binned into one of several categories. If the Keima561^{high} punctum stemmed from a larger Keima440^{high} mitochondrion, it was considered "new mitophagy". If the punctum broke away from a different, larger Keima561^{high} mitolysosome, it was considered a "split mitolysosome". If the punctum migrated into the imaging volume near the edges, it was considered "from outside" (Figure 4B). Out of 381 objects, 325 were stable from the beginning to the end of the imaging period, 11 migrated from outside, only 3 were new mitophagy (Figure 4C, * and yellow surface object), and 37 puncta split from larger mitolysosomes (Figure 4D, *). Thus, *de novo* mitophagy rapidly occurs during this stage of fasting and accounts for some of the new, small mitolysosomes, but mitolysosome fission is the predominant source of the small mitolysosomes, which appear during advanced fasting.

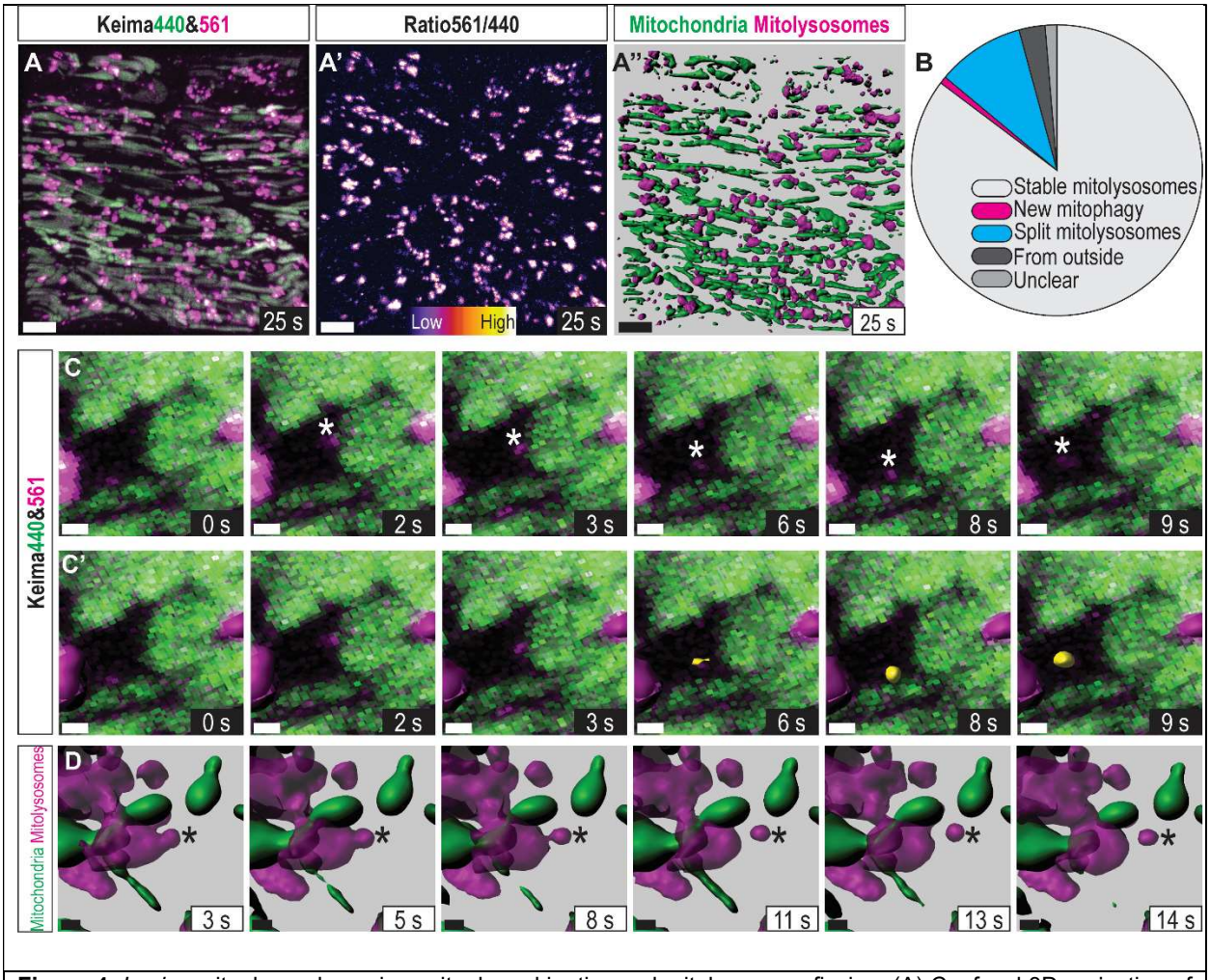

Figure 4. *In vivo* mitophagy dynamics: mitophagy kinetics and mitolysosome fission. (A) Confocal 3D projection of the imaging volume in Movie 2. Images of skeletal muscle in a 7 dpf larva during advanced nutrient deprivation. Images were continuously acquired, finishing each volume approximately once per second and tracking skeletal muscle mitochondria in ~2 cell-deep volume for 28 s. (A') Ratiometric image isolating mitolysosomes. (A'') Isosurface rendering of mitochondria (green) and mitolysosomes (magenta) used to track mitochondria, mitophagy, and mitolysosome fission. Scale, 10 μm. (B) Classification of each Keima561^{high} object revealing that approximately 85% were stable, 1% were newly formed, and 10% split from existing, larger mitolysosomes within the 28 s timeframe. The remaining mitolysosomes were pre-existing or translocated from outside the imaging volume. (C) Zoomed timeseries of a representative "new mitophagy" event marked with (*). (C') Same as (C) with isosurface objects for stable mitolysosomes (magenta) and the new Keima561^{high} object (yellow). Scale, 1 μm. (D) Isosurface representation of a splitting mitolysosome (*). Scale, 1 μm.

Fasting-induced mitophagy occurs piece-by-piece

It is unknown whether *in vivo* mitophagy occurs via a wholesale or piecemeal mode. To investigate how GFP-Lc3-labeled organelles interact with mitochondria *in vivo*, we performed time-lapse analysis in *Tg(CMV:GFP-Lc3)^{zf155};(ubi:mito-Keima)* larvae at ~1 min/frame time

resolution. Isosurface renderings identified and tracked the different organelle structures in three dimensions. Mitophagy events (transition from Keima440^{high} to Keima561^{high}) were captured and occurred at discrete points along the filamentous mitochondria, often near the poles. Interestingly, we never observed massive mitochondrial fragmentation followed by mitophagy, indicating the wholesale mode of mitophagy is not active in this context. In contrast, we detected mitophagy occurring at discrete contact points between Lc3 and filamentous mitochondria (Figure 5A; 5A', *; Movie 3), indicative of piecemeal mitophagy.

Intriguingly, the Keima561^{high} mitolysosomes colocalized extensively with EGFP-Lc3 signal, indicating that EGFP-Lc3 labels both autophagosomes and autolysosomes in this system (Figure 1C). To differentiate acidified autolysosomes from autophagosomes, *Tg(CMV:GFP-Lc3)^{zf155};(ubi:mito-Keima)* larvae were stained with LysoTracker Deep Red and object-based colocalization image analysis was performed. This analysis required activation of Keima with a 488 nm laser, causing additional overlap between the neutral/basic and acidic Keima signals. To accommodate for this, we defined healthy mitochondria by the Keima488/561 signal ratio and generated surface objects for healthy mitochondria, mitolysosomes, EGFP-Lc3 positive objects, and LysoTracker positive objects (Figure 5B). First, object-based colocalization was employed to determine which EGFP-Lc3^{+} objects were autolysosomes—in contact with a LysoTracker^{+} object—or autophagosomes—not in contact with a LysoTracker^{+} object (Figure 5C). Autolysosomes were substantially larger in volume than autophagosomes (Figure 5D). Remarkably, nearly all autolysosomes contained Keima561/488^{high} objects, classifying them as automitolysosomes, whereas nearly all autophagosomes did not (Figure 5E). Approximately 45% of autophagosomes and ~68% of autolysosomes were in direct contact with healthy mitochondria, supporting our observation that mitophagy occurred at discrete contact points between EGFP-Lc3^{+} organelles and healthy mitochondrial filaments.

Mitochondrial protein aggregates can be cleared via a piecemeal mitophagy mechanism in cultured cells, and knockout of Drp1 impaired mitochondrial fission and led to wholesale mitophagy (Burman et al., 2017). We hypothesized that inhibition of Drp1 could similarly induce a wholesale mitophagy response *in vivo*. Thus, we introduced a heat shock inducible, dominant negative Drp1(K38A)-2A-nlsEGFP (DN-Drp1) construct (Smirnova et al., 1998) to ubi:mito-Keima larvae and induced expression in the resulting mosaic animals during fasting. At 7 dpf, cells expressing DN-Drp1 (identified by nuclear EGFP expression) had altered mitochondrial morphology with increased connections between filaments, indicating that expression of DN-Drp1 functionally reduced mitochondrial fission (Figure 5G, arrows). Interestingly, mitophagy was not diminished in these cells compared to neighboring wild type (WT) $EGFP^{-}$ cells, and in some $EGFP^{+}$ cells, $Keima561^{high}$ signal occurred in a pattern indicative of wholesale mitophagy of large mitochondrial filaments (Figure 5G). Together, these results indicate fasting-induced mitophagy in skeletal muscle occurs piecemeal, and that Drp1 inhibition does not prevent mitophagy but can induce wholesale recycling of mitochondrial filaments.

Mitochondrial substructures can also be removed piecemeal by an Lc3-independent mechanism utilizing mitochondria-derived vesicles (MDVs) (Cadete et al., 2016; Sugiura et al., 2014). 88.5% of mitolysosomes, however, colocalized within 0.5 μm of an $Lc3^{+}$ object (Figure 5I). Thus, in fasted muscle, the MDV pathway may not play a major role in mitochondrial recycling. In sum, mitophagy in fasted skeletal muscle occurs primarily by a piecemeal mechanism utilizing $Lc3^{+}$ organelles.

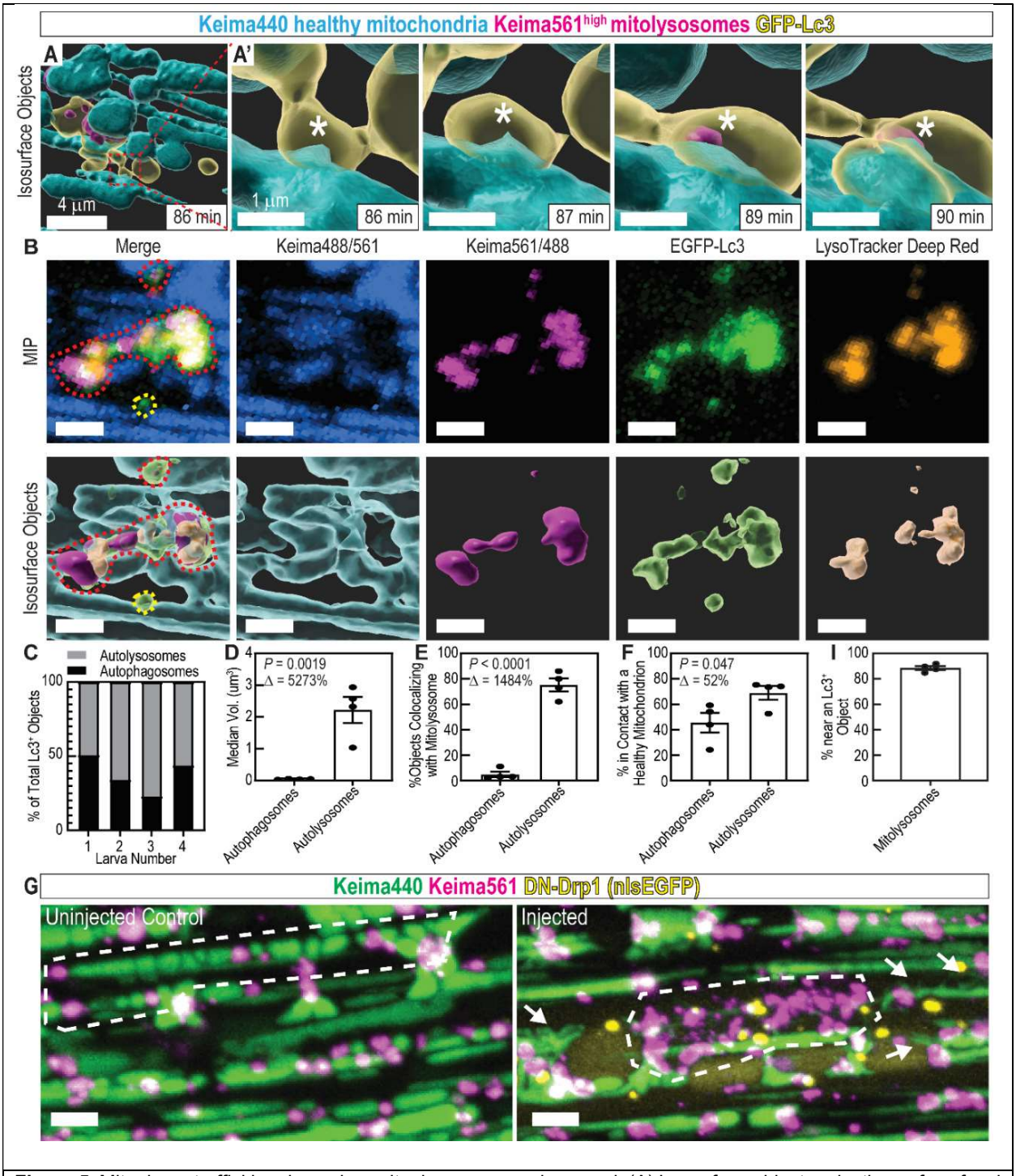

Figure 5. Mitophagy trafficking dynamics: mitophagy occurs piecemeal. (A) Isosurface object projections of confocal time-lapse imaging of fasted skeletal muscle in 5 dpf ubi:mito-Keima larva. Scale, 4 µm. (A') Inset of (A); mitophagy occurs piecemeal. An EGFP-Lc3^{+} surface is interacting with a Keima440^{high} filamentous mitochondrion (86 min; *). Then, a small portion of the longer filamentous mitochondrion becomes Keima561^{high}, indicating pH change and mitophagy (89 min; *). Scale, 1 µm. (B) MIP and isosurface object representations displaying healthy mitochondria (Keima488/561), mitolysosomes (Keima561/488), EGFP-Lc3^{+} objects, and LysoTracker Deep Red^{+} objects. Red outline highlights an autolysosome containing degraded mitochondria. Yellow outline highlights an autophagosome containing no mitochondria. Scale, 2 µm. (C) Classification of EGFP-Lc3^{+} objects as autophagosomes or

autolysosomes. Those in contact with LysoTracker^{+} objects are autolysosomes, and the remaining are autophagosomes. (D) Volume quantification of autophagosomes and autolysosomes. (E) Colocalization analysis between mitolysosomes (Keima561^{high} objects) and autophagosomes or autolysosomes. (F) Colocalization analysis between healthy mitochondria and autophagosomes or autolysosomes. (D-F,I) Data shown are mean ± SEM. *P*, unpaired, two-tailed Student's t test. Δ, percentage change between autophagosomes and autolysosomes. *n* = 4 individual 6 dpf larvae. (G) MIP of 7 dpf ubi:mito-Keima larvae injected with an inducible DN-Drp1 construct. Compare the piecemeal mitophagy pattern in the control to the wholesale mitophagy pattern in the injected (white dotted outlines). Mitochondrial morphology is also altered in DN-Drp1-injected larvae (arrows). Scale, 4 μm. (I) Colocalization analysis between mitolysosomes and Lc3^{+} objects.

Hif activation induces mitophagy

Tissue hypoxia (ischemia) occurs in muscle during in exercise and other physiological and pathophysiological conditions (Ferdinand and Roffe, 2016; Lee et al., 2019; Leermakers and Gosker, 2016). This stress leads to mitochondrial damage, production of excess reactive oxygen species, and mitophagy (Kaelin and McKnight, 2013). We used the zebrafish mitophagy reporter system to dissect the effects of hypoxia and activation of the Hif pathway on muscle mitophagy (Figure 6A). To avoid fasting-induced mitophagy as a confounding variable, we examined larvae younger than 5 dpf. To induce physiological hypoxia, zebrafish larvae were raised in hypoxic fish water within a hypoxia chamber (4.7% O_2) from 77-96 hpf, causing death in 11 of 35 larvae, indicative of the substantial hypoxic stress induced by this approach. Surviving larvae had a significant increase in mitophagy in skeletal muscle (Figure 6B). Next, we tested whether chemical activators of Hif signaling induced mitophagy in skeletal muscle. The PHD inhibitor dimethyloxalylglycine (DMOG) has been validated to induce Hif activation in similarly aged zebrafish larvae (Elks et al., 2013; Iliopoulos et al., 1996; Ivan et al., 2001). Fish exposed to DMOG from 3-4 dpf exhibited robust mitophagy compared to controls (Figure 6C). This result was confirmed by exposing zebrafish to FG-4592 (Roxadustat), a chemically dissimilar PHD inhibitor evaluated for FDA approval, which caused a similar increase in mitophagy (Figure 6D). Genetic knockdown of *vhl* using a previously validated MO (Harris et al., 2013) also induced mitophagy at 3 dpf (Figure 6E). To test whether Hif activation alone was sufficient to induce mitophagy in skeletal muscle in a cell autonomous manner, dominant active Hif (*DA-hif1ab*) (Elks et al., 2011)

and nuclear-localized EGFP were expressed under the control of the muscle-specific *unc45b* promoter (Berger and Currie, 2013). This resulted in mosaic expression of nuclear EGFP, indicating the cells expressing DA-hif1ab, which could be compared to neighboring $EGFP^-$, WT cells within the same animal. $EGFP^+$ cells had high levels of mitophagy, whereas surrounding $EGFP^-$ cells had little-to-no mitophagy similar to uninjected controls (Figure 7F). Together, these results confirm that hypoxia and Hif activation elicit mitophagy in a cell-autonomous fashion and further demonstrate the utility of our model for characterizing the physiological regulation of mitophagy.

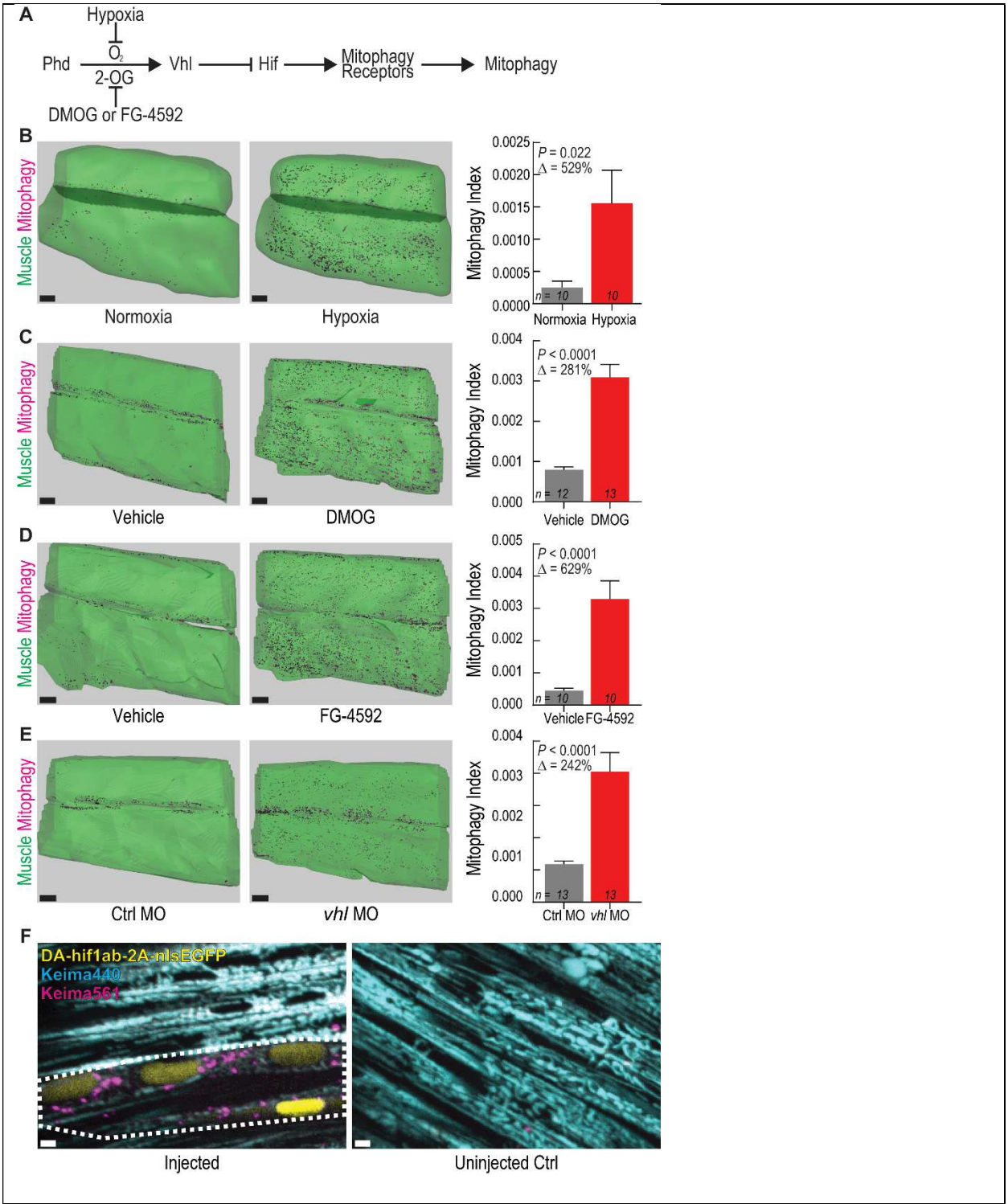

Figure 6. Activating hypoxia-inducible factor (Hif) signaling induces mitophagy in skeletal muscle. (A) Schematic of Hif signaling pathway. 2-OG, 2-oxoglutarate. (B-E) Isosurface renderings and Mitophagy Index quantification in skeletal muscle of 4 dpf ubi:mito-Keima zebrafish exposed to (B) 4.7% oxygen (hypoxia), (C) 60 μM DMOG, or (D) 10 μM FG-4592 from 3-4 dpf. (E), Isosurface renderings and quantification of mitophagy in skeletal muscle of 3 dpf zebrafish injected with control MO (Ctrl) or *vhl* antisense MO. Scale bars, 30 μm. Data shown are mean + SEM. *P*, unpaired, two-tailed Student's t test. Δ, percentage change of experimental cohort to control cohort. *n* indicates

number of larvae in each cohort. (F) Confocal microscopy images of 4 dpf ubi:mito-Keima expressing dominant active (DA) *hif1ab* in a mosaic fashion. Keima440 is cyan. Keima561 is magenta. Nuclear EGFP is yellow and indicates the cells that express *DA-hif1ab*. White dotted line outlines two adjacent myotubes expressing *DA-hif1ab* and undergoing mitophagy. Scale bars, 2 μm.

Disruption of *bnip3* alone diminishes Hif-induced mitophagy

Next, we used the volumetric *in vivo* mitophagy quantification method and high-efficiency genome editing to dissect the molecular mechanisms required for Hif-induced mitophagy in vertebrate skeletal muscle. As a positive control, we tested whether the mitophagy signal resulting from DMOG exposure was dependent on macroautophagy by assessing dependence on Vps34, which is necessary for autophagosome formation and vital for macroautophagy. A cohort of DMOG-exposed larvae (both ubi:mitoKeima and ubi:mito-GR in independent experiments) was treated with the Vps34 inhibitor SAR405 (Ronan et al., 2014). Exposure to SAR405 abrogated DMOG-induced mitophagy (Figure 7A and Figure 7—figure supplement 1), indicating that macroautophagy is vital for Hif-induced mitophagy.

HIF-induced mitophagy is thought to rely on the function of specific mitophagy receptors BNIP3, BNIP3L (NIX), and FUNDC1, which contain LC3-interacting regions (LIRs) (Birgisdottir et al., 2013; Yoo and Jung, 2018). To test the requirement of these factors for Hif-induced mitophagy, *bnip3*, *bnip3la* (*nix*), and *fundc1* were disrupted in F0 larvae by CRISPR methodology, an established and rapid method to assess loss of gene function (Figure 7—figure supplement 2) (Burger et al., 2016). Surprisingly, larvae injected with a *bnip3*-targeted CRISPR cutter (CC) reliably exhibited dramatic reduction in DMOG-induced mitophagy, indicating that singular disruption of the *bnip3* locus diminishes Hif-induced mitophagy in vertebrate skeletal muscle (Figure 7B and Figure 7—figure supplement 3). Disruption of other receptors implicated in hypoxia-induced mitophagy, specifically *bnip3la* (*nix*) (Figure 7C) and *fundc1* (Figure 7D), had no effect on DMOG-induced mitophagy. These results indicate that *bnip3*, a single mitophagy receptor, is necessary for the Hif-induced mitophagy response in vertebrate skeletal muscle.

BNIP3 has been shown to interact directly with PINK1, promoting mitophagy via the PINK1-PARKIN pathway (T. Zhang et al., 2016), and a study in flies showed *Pink1* to be necessary for hypoxia-induced mitophagy (Kim et al., 2019). However, there were no significant differences in Hif-induced mitophagy in skeletal muscle between fish homozygous for an established *pink1* null allele (gi2) (Zhang et al., 2017) and their WT or heterozygous siblings (Figure 7*E*). Additionally, larvae injected with a validated *pink1* MO (Priyadarshini et al., 2013) showed no difference in DMOG-induced mitophagy compared to controls (Figure 7—figure supplement 4). Further, disruption of *prkn* had no effect (Figure 7F and Figure 7—figure supplement 3). In sum, disruption of a single Hif-responsive mitophagy receptor locus *bnip3* mitigates Hif-induced mitophagy in skeletal muscle, independent of the *pink1-prkn* pathway (Figure 7G).

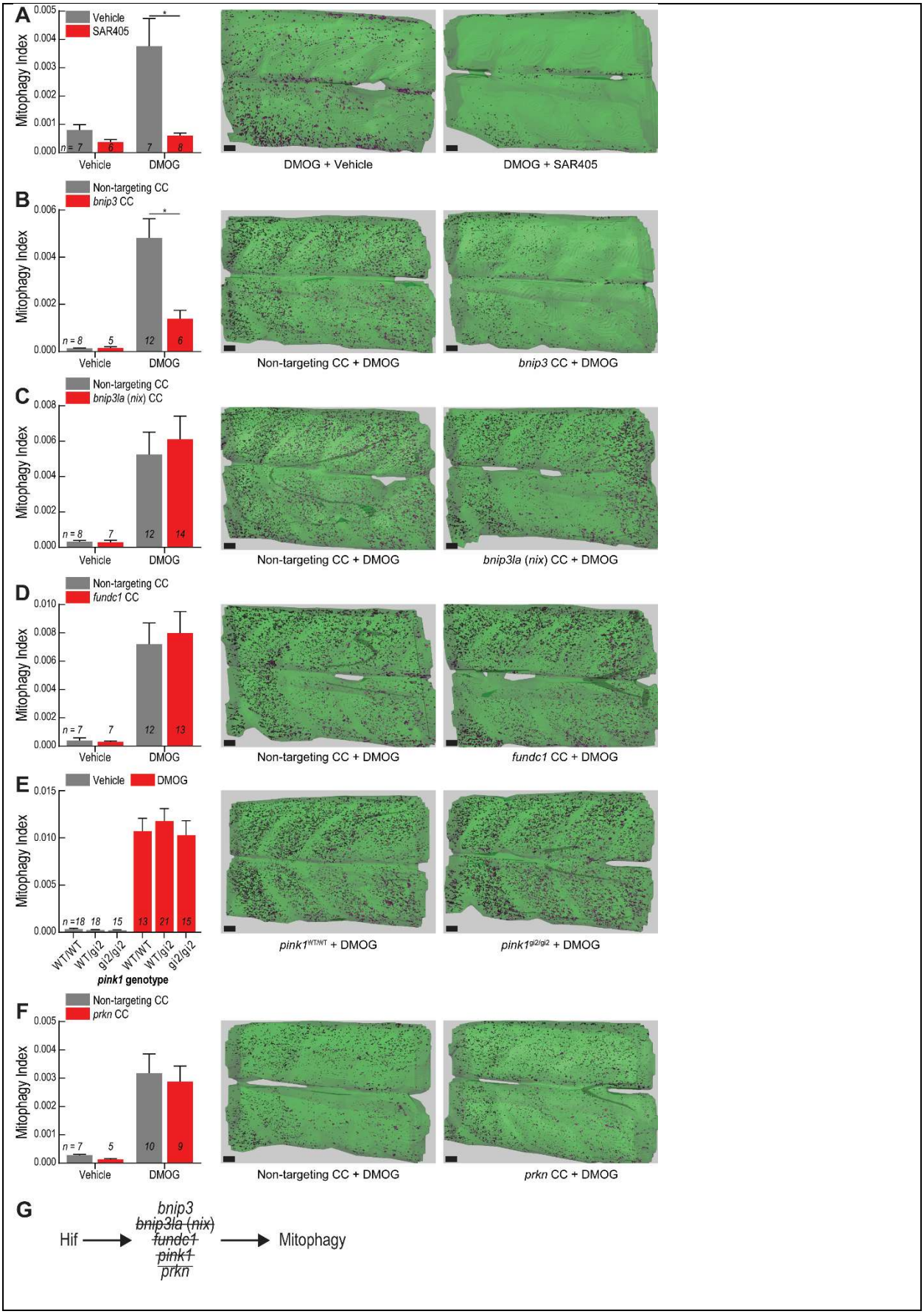
A
Vehicle
SAR405
Mitophagy Index
0.005
0.004
0.003
0.002
0.001
0.000
n = 7
6
7
8
Vehicle
DMOG
DMOG + Vehicle
DMOG + SAR405
B
Non-targeting CC
bnip3 CC
0.006
0.004
0.002
0.000
n = 8
5
12
6
Non-targeting CC + DMOG
bnip3 CC + DMOG
C
Non-targeting CC
bnip3la (nix) CC
0.008
0.006
0.004
0.002
0.000
n = 8
7
12
14
Non-targeting CC + DMOG
bnip3la (nix) CC + DMOG
D
Non-targeting CC
fundc1 CC
0.010
0.008
0.006
0.004
0.002
0.000
n = 7
7
12
13
Non-targeting CC + DMOG
fundc1 CC + DMOG
E
Vehicle
DMOG
0.015
0.010
0.005
0.000
n =18
18
15
13
21
15
WT/WT
WT/gi2
gi2/gi2
pink1 genotype
pink1WT/WT + DMOG
pink1gi2/gi2 + DMOG
F
Non-targeting CC
prkn CC
0.005
0.004
0.003
0.002
0.001
0.000
n = 7
5
10
9
Non-targeting CC + DMOG
prkn CC + DMOG
G
Hif
bnip3
bnip3la (nix)
fundc1
pink1
prkn
Mitophagy

Figure 7. Disrupting *bnip3* but not *bnip3la* (*nix*), *fundc1, pink1*, or *prkn* mitigates Hif-induced mitophagy. (*A*) Mitophagy Index quantification of larvae treated with 100 μM DMOG or vehicle (DMSO) and 20 μM SAR405 or vehicle (DMSO). Representative isosurface rendering images show the effect of SAR405 treatment on DMOG-induced mitophagy. (*B-D*,*F*) Mitophagy Index quantification and representative isosurface rendering images of DMOG-induced mitophagy in larvae injected with CRISPR cutters (CC) targeting (*B*) *bnip3*, (*C*) *bnip3la* (*nix*), (*D*) *fundc1*, or (*F*) *prkn*. Scale bars, 20 μm. (*E*) Mitophagy Index quantification and representative isosurface rendering images of DMOG-induced mitophagy in larvae carrying a null *pink1* allele (gi2) and siblings. (*A-F*) Data shown are mean + SEM. *P<0.01, two-way ANOVA with Holm-Sidak's multiple comparisons test. Each comparison between vehicle- and DMOG-treated samples was also significant (P<0.05) except in (*A*) vehicle controls to DMOG+SAR405 and (*B*) vehicle controls to DMOG + *bnip3* CC. Scale, 20 μm. See Figure 8-figure supplement 2, 3 for replicates and full statistical analyses. *n* indicates number of larvae in each cohort. (*G*) Schematic demonstrating Hif-induced mitophagy requires *bnip3* but not *bnip3la* (*nix*), *fundc1*, *pink1*, or *prkn*.

DISCUSSION

In this study, we reveal fundamental characteristics of *in vivo* mitophagy during normal organ development and physiological stress using mitophagy biosensor zebrafish combined with precise image analysis methods. Basal mitophagy occurred in many developing organs. In fasted skeletal muscle, mitolysosomes initially increased in size, followed by a period of concurrent mitophagy and mitolysosome fission. Time lapse imaging revealed fasting-induced mitophagy occurred *in vivo* via a piecemeal mechanism. Hypoxia and Hif-activation induced mitophagy in skeletal muscle. Hif-induced mitophagy required *bnip3* function, but *pink1*, *prkn*, *bnip3la* (*nix*), and *fundc1* are dispensable. In sum, these results reveal *in vivo* subcellular dynamics and molecular mechanisms regulating physiological-stress induced mitophagy.

Transgenic animals expressing mitophagy reporter constructs have begun to reveal basal mitophagy levels *in vivo*. Murine studies demonstrated that adult tissues with high metabolic demands—brain, liver, kidney, spleen, skeletal muscle—have high basal mitophagy levels (McWilliams et al., 2016; Sun et al., 2015). Similarly, studies in flies show basal mitophagy in the central nervous system, epidermis, and muscle (Lee et al., 2018). The developing mouse heart and kidney display high mitophagy (McWilliams et al., 2016), but more extensive developmental analyses have not been performed. Recently, *nipsnap1* mutant zebrafish were found to have decreased basal mitophagy in skin and defects in dopamine neuron development (Abudu et al.,

2019). Our study detects widespread mitophagy in embryonic and larval zebrafish during the development of many organs, including several previously unrecognized, such as the spinal cord, notochord, vasculature, pancreas, and liver.

The *in vivo* dynamics of mitophagy have not been previously studied via live imaging. The canonical mitophagy sequence involves mitochondrial fission occurring prior to engulfment by preformed autophagosomes (Anding and Baehrecke, 2017). Conversely, mitophagy receptors localized to the point of damage on mitochondria can recruit the ULK1 complex and initiate autophagosome biogenesis locally (Vargas et al., 2019). In fasted muscle, we found that many autophagosomes ($Lc3^{+}$ objects not in contact with $LysoTracker^{+}$ objects) and most autolysosomes were in direct contact with intact mitochondrial filaments, suggesting that much of autophagosome biogenesis may occur locally, and that much of the fasting-induced autophagy occurring is mitophagy. Time lapse analysis indicated that mitophagy, as defined by transition from $Keima440^{high}$ to $Keima561^{high}$, occurred near these points in a piecemeal fashion. This also suggests that the process of autophagosome acidification in skeletal muscle is rapid during this advanced stage of fasting. The piecemeal nature of mitophagy in skeletal muscle may be an adaptation necessary to allow for muscle mitochondria to exist as large, fused networks to more efficiently generate ATP and other metabolites (Friedman and Nunnari, 2014; Romanello and Sandri, 2013). Indeed, in mice, skeletal muscle-specific deletion of Opa1, a protein necessary for inner mitochondrial membrane fusion, leads to fragmented mitochondria, muscle degradation, mitochondrial dysfunction, and mitophagy defects (Rodríguez-Nuevo et al., 2018). Our observations also fit well with a recent report demonstrating that mitochondrial division occurs concurrently with autophagosome formation in yeast and HeLa cells (Yamashita et al., 2016) It will be important to determine why mitophagy occurs at specific points along the mitochondrial filament *in vivo*. The topology and shape of mitochondria have been implicated as driving forces for starvation-induced mitophagy in osteosarcoma cells (Zhou et al., 2019). Differential

segregation and phosphorylation of mitochondrial matrix proteins was also shown to determine mitophagy rates of different mitochondrial proteins (Abeliovich et al., 2013; Kolitsida et al., 2019). It is exciting to speculate that different mitochondrial proteins could segregate to specific subdomains and dictate the location of mitochondrial fission and mitophagy.

Different types of piecemeal selective autophagy have been discovered. A LIR-containing protein TEX264 was recently demonstrated to be necessary for piecemeal selective autophagy of the ER in HEK293 cells (Abeliovich et al., 2013), proving that receptor-mediated selective autophagy can also occur piecemeal. In HeLa cells, a homeostatic piecemeal mitophagy mechanism relies on p62 and LC3C but not PINK1-PARKIN to regulate oxidative phosphorylation (Le Guerroué et al., 2017). A recent study explored mitophagy kinetics using mild oxidative stress to induce more physiological levels of mitophagy in cultured rat neurons, indicating that mild mitochondrial stresses may better model the *in vivo* process (Evans and Holzbaur, 2020). It is possible the wholesale mechanism only occurs during autophagic cell death or is primarily an *in vitro* event caused by unphysiologically high mitochondrial stress levels. It will be important for future work to analyze the mitophagy trafficking dynamics and mechanisms *in vivo* in other cell types and under different physiological stresses to uncover endogenous mitophagy kinetics and to determine if every instance of mitophagy occurs via a piecemeal mechanism.

Many genes have been implicated in both ubiquitin-dependent and ubiquitin-independent mitophagy (Anding and Baehrecke, 2017; Harper et al., 2018; Rodger et al., 2018). These studies, however, were primarily performed in cell culture with limited confirmation of conserved mechanisms *in vivo*. BNIP3, BNIP3L (Nix), and FUNDC1 have all been linked to hypoxia-induced mitophagy and HIF signaling (Yoo and Jung, 2018). They contain domains to localize them to the mitochondrial outer membrane, and LIRs, which bind to LC3 and recruit autophagosomal membranes (Birgisdottir et al., 2013). BNIP3 mediates hypoxia-induced mitophagy in MEFs and murine lung tissue (Zhang et al., 2008). In murine skeletal muscle, FoxO

signaling causes fasting-induced autophagy via BNIP3, although neither mitophagy nor hypoxia were analyzed (Mammucari et al., 2007). BNIP3 also facilitates mitophagy in murine cortical neurons in a stroke model (Shi et al., 2014) and in murine hearts and HL1 cardiac muscle cells after myocardial ischemia/reperfusion injury (Hamacher-Brady et al., 2007). BNIP3L (NIX) is linked to hypoxia-induced mitophagy in ischemic brain injury and heart ischemia/reperfusion injury in mice (Yuan et al., 2017). FUNDC1 is thought to facilitate hypoxia-mediated mitophagy in HeLa cells (Chen et al., 2014; Liu et al., 2012), several murine tissues including platelets, liver, heart, and muscle (W. Zhang et al., 2016), and also in cardiac ischemia/reperfusion injury (Zhou et al., 2017). In light of these studies, it might be expected that multiple, redundant mitophagy receptors facilitate the hypoxia response in skeletal muscle. In contrast, we found that only disruption of *bnip3* mitigated Hif-induced mitophagy in skeletal muscle, whereas disruption of *bnip3la* (*nix*) or *fundc1* had no effect. Our results add mechanistic insight into the tissue- and stress-dependent contexts for vertebrate mitophagy mechanisms.

There is conflicting evidence for how BNIP3 induces mitophagy. In MEFs, BNIP3 functions by facilitating the release of Beclin-1 from Bcl-2, allowing Beclin-1 to initiate autophagy independent of the PINK1-PARKIN pathway (Zhang et al., 2008). However, a separate study in MEFs and HEK293 cells showed BNIP3 interacted with and stabilized PINK1, which recruited PARKIN to the mitochondrial outer membrane and initiated PINK1-PARKIN-dependent mitophagy (T. Zhang et al., 2016). Separately, *Pink1* was shown to be necessary for hypoxia-induced mitophagy in flies (Kim et al., 2019). In zebrafish, however, we tested an established mutant *pink1* allele, *pink1* morphants, and *prkn* disruption via CRISPR and found that none of these interventions prevented Hif-induced mitophagy in zebrafish muscle. This supports the conclusion that in vertebrates, *bnip3*-induced mitophagy is independent of the Pink1-Parkin ubiquitination system. In flies, *Pink1* mutation causes muscle degeneration (Clark et al., 2006; Park et al., 2006; Yang et al., 2006), and BNIP3 overexpression can rescue the phenotype (T.

Zhang et al., 2016). In humans (Gasser, 2009), monkeys (Yang et al., 2019), mice (McWilliams et al., 2018), and zebrafish (Zhang et al., 2017) there is no evidence of direct muscle degeneration due to PINK1 mutation, indicating that there are important differences between vertebrate and invertebrate mitophagy mechanisms. Because there are few yeast homologs to vertebrate mitophagy receptors (Mao et al., 2011) and due to the observed differences in mitophagy mechanisms between vertebrate and invertebrate models, analysis of mitophagy reporter zebrafish provides a unique avenue toward deeper understanding of mitochondrial quality control dynamics and mechanisms. In summary, our study revealed widespread mitophagy during development, fundamental piecemeal mitophagy dynamics during fasting, and that hypoxia-induced mitophagy is dependent on *bnip3*.

MATERIALS AND METHODS

Animal Studies: Zebrafish (*Danio rerio*) were maintained according to institutional animal care and use committee (IACUC-BIDMC #506-2015) protocols. Adult fish and larva were raised at 28.5 ^{o}C. All studies were performed in larval zebrafish before sex can be determined, and therefore sex was not taken into consideration. All embryos and larvae were raised and experimentally treated in E3 salt solution. For experiments involving larval feeding, embryos were provided live paramecia and larval AP-100 fish food (Zeigler) *ad libitum*.

Molecular Cloning and Transgenesis: Transgenic lines *Tg(ubi:mito-Keima,cryaa:Cerulean)*, *Tg(ubi:mito-GR)*, and *Tg(fabp10a:mito-GR)* were generated using *tol2* transgenesis (Her et al., 2003; Mosimann et al., 2011; Mosimann and Zon, 2011). Plasmids generated or used are listed in the Key Resources Table. Middle entry vector pENTR:mito-Keima was generated via PCR using pHAGE mt-Keima IRES Puro as template and pENTR/D-TOPO kit (Invitrogen) following manufacturer's instructions. A Gateway reaction using LR Clonase II Plus (Invitrogen) generated the pTol2-*ubi:mito-Keima,cryaa:Cerulean* vector following manufacturer's instructions. Middle

entry vector pME-mito-GR was generated using BP Gateway cloning using pCLBW cox8 EGFP mCherry (Rojansky et al., 2016) and pDONR221 (Invitrogen) using Gateway BP Clonase II Enzyme (Invitrogen) mix following manufacturer's instructions. LR Gateway cloning was used to generate pTol2-*ubi:mito-GR*, and pTol2--*2.8fabp10a:mito-GR*. Middle entry vector pENTR-DA-hif1ab(noStop) was generated using PCR to amplify DA-hif1ab minus the Stop codon from a plasmid containing DA-hif1ab (Elks et al., 2011), which was a gift from Phil Elks. Middle entry vector pENTR-DN-Drp1(noStop) was generated similarly using a plasmid containing Drp1(K38A) (Smirnova et al., 1998). LR Gateway reactions generated the pTol2--*503unc45b:DA-hif1ab-2A-nlsEGFP,cryaa:mCherry* and pTol2-*hsp70l:DN-Drp1-2A-nlsEGFP,cryaa:mCherry* vectors following manufacturer's instructions. *Tol2* mRNA was synthesized using mMessage mMachine SP6 *In vitro* Transcription kit (Invitrogen) following the manufacturer's instructions. To generate stable transgenic lines, 1-cell stage TU embryos were injected with the transgenesis vector and *tol2* transposase mRNA. Positive embryos were screened either for cyan fluorescent lenses (ubi:mito-Keima) or for EGFP fluorescence (ubi:mito-GR and fabp10a:mito-GR) and raised to adulthood. F0 adults were outcrossed to TL mates, the F1 generation clutches were screened for bright fluorescence, and potential founders were raised. Potential F1 founders were outcrossed again to TU or TL mates and screened for bright fluorescence and 1:1 ratio of WT to transgenic offspring indicative of single copy insertion (Mosimann and Zon, 2011). All experiments were performed on F2 or later generation larvae.

Fasting and Feeding Protocols: Fasted fish were kept in E3 medium cleaned of any dead larvae and shed chorions. Fed controls were provided live paramecia and AP100 dry larval diet (Zeigler) *ad libitum*. For heat shock induction of mito-Keima, larvae were placed into a 50 mL conical tube with 35 mL of E3 then incubated for 45 min at 38 ^{o}C before being returned to room temperature E3.

Hypoxia and Chemical Treatments: For MitoTracker analysis, larvae were exposed to 1 μM MitoTracker Green FM (Cell Signaling Technology) overnight in E3, washed in E3 twice, and prepared for imaging. For LysoTracker analysis, larvae were exposed to 1 μM LysoTracker Green DND-26 (Cell Signaling Technology) or LysoTracker Deep Red (Thermo Fisher Scientific) overnight in E3, washed in E3 twice, and prepared for imaging. For all drug treatment experiments, single clutches were used and split between experimental groups. If additional embryos were necessary, two clutches from sibling breeding pairs were combined and mixed to split randomly. For hypoxia experiments, E3 was reduced to approximately 1.7 mg/L O_2 by bubbling in a mixture of 95% N_2 and 5% O_2 for about 10 minutes. The larvae E3 in a 10 cm dish was replaced with about 40 mL of the hypoxic water, and the dish was moved to a hypoxia chamber, which was then flushed with the same mixture of 95% N_2 and 5% O_2 for about 10 minutes until an O_2 sensor (DO210, Extech Instruments) read 4.7%. The chamber was sealed and moved into the 28.5 ^{o}C incubator. For chemical hypoxia experiments, larvae were exposed to 60 μM or 100 μM DMOG (Tocris) or 10 μM FG-4592 (Cayman Chemical) in E3 from about 70 hpf to 98 hpf. The exception is the *pink1* MO experiment for which the treatment window was from 48-72 hpf. This is because MO knockdown is most effective during the first 3 dpf before additional cell divisions dilute the MO (Bill et al., 2009). For SAR405 experiments, larvae were split into cohorts receiving vehicle (DMSO; Sigma Aldrich) or 100 μM DMOG and then those cohorts were split into cohorts receiving additional vehicle (DMSO) or 10 μM SAR405 (EMD Millipore). The SAR405 treatment experiment and each high-efficiency CRIPSR experiment was replicated.

Confocal Microscopy: Microscopy was performed using an inverted Ti2 (Nikon) microscope equipped with a Yokogawa CSUW1 spinning disc confocal unit, a CFI Apo LWD Lambda S 40XC WI (1.15 N.A.) objective lens (Nikon), and a Zyla 4.2+ sCMOS camera (ANDOR). Keima images were captured by exciting with 440 nm laser light and 561 laser light with ET Cy3/TRITC emission filter (Chroma) in triggered acquisition mode. Mito-GR images were captured using 488 nm laser

light and 561 nm laser light with ET FITC/TRITC dual emission filter (Chroma) in triggered acquisition mode. For MitoTracker Green, LysoTracker Green, EGFP-Lc3, and nlsEGFP imaging, 488 nm excitation was utilized with a 525/36 FITC emission filter (Chroma). For Lysotraker Deep Red, a similar microscope equipped with a 640 nm laser and ET705/72m emission filter (Chroma) was utilized. For images involving both Keima and EGFP signal, the EGFP images were uniformly frame-shifted (Nikon Elements) based on control images to account for the shift caused by using different dichroic mirrors. For the *in vivo* mitophagy dynamics time-lapse imaging (Figure 4 and Movie 2), an iXon Life 888 EMCCD (ANDOR) was used for its increased light sensitivity and frame rate capacity, allowing greater time resolution. Larvae were anesthetized with 0.16 mg/mL Tricaine-S (Western Chemical, Inc.) and mounted on glass-bottom dishes (MatTek) in 0.8% low-melt point agarose in E3 containing Tricane. After the agar solidified, additional E3 + Tricane was added to keep the gel hydrated during imaging. For skeletal muscle imaging, the collection volume was centered on the ninth and tenth myotomes. For all quantitative experiments, images of all samples were collected with identical laser power, gain and exposure time.

Image Analysis: All mito-Keima image analysis was conducting using Imaris (Bitplane) software with either FIJI (ImageJ) or MATLAB (MathWorks) plugins to enable image mathematics. Raw images from Nikon Elements (.nd2) were converted to Imaris (.ims) file format using Imaris Image Converter (Bitplane) and imported to Imaris. A surface mask was drawn manually using the Surfaces function to segment muscle tissue away from skin. A ratiometric image (FIJI or MATLAB) was generated by changing the data type to 32 Bit Float and applying the following equation: (Keima561 channel) / (Keima440 channel + 150). The 150 addition ensures that areas of low signal from both Keima561 and Keima440 were excluded. The ratiometric image normalizes for the decrease in signal intensity as imaging depth into the tissue increases and for small intensity differences between samples. Then, an isosurfaces thresholding algorithm was applied to the ratio channel, with 0.15 μm surface grain (smoothing) to eliminate noise, using a

threshold value determined for each experiment from images of control fish. A size cutoff removed objects smaller than 2 voxels to eliminate additional noise. Obviously spurious surfaces were removed manually. Rarely, individual slices were removed from z-stack images to account for fish movement, which caused edge artifacts in some ratio images. Mitolysosome density was determined by dividing the number of ratio surface objects by the total tissue surface volume. Mitophagy index was determined by dividing the sum of all ratio surface object volumes by the total tissue surface volume. For mito-GR images, a deconvolution algorithm (Imaris) to adjust for the behavior of light of differing emission wavelengths (green and red) was used reduce edge artifacts. Object tracking in time-lapse microscopy (Figure 4 and Movie 2) was performed using Imaris software (Bitplane). Mitophagy isosurface masks were generated as described above. Mitochondria surfaces were generated using a 0.325 μm surface grain (smoothing), background subtraction (diameter largest sphere = 1.219 μm), a manually determined florescence intensity threshold, and a size cutoff eliminating objects smaller than 15 voxels. Object tracking was performed on ratio surface objects, using autoregressive motion, a maximum distance of 1.003 μm, a maximum gap size of 3 (without gap filling), and a track duration minimum of 5.534 s. We manually assessed each newly formed mitophagy isosurface object, defined as a $Ratio^{high}$ tracked object that was not present at time zero; other mitophagy objects were considered stable. Using a combination of microscopy views, new objects were manually classified as new mitophagy, split mitolysosomes, or from outside. For lysosome size analysis, LysoTracker Green z-stack images were acquired covering 8.8 μm depth within the skeletal muscle of the fish and analyzed using FIJI. First, background subtraction using 50 μm rolling ball was performed, then a maximum intensity projection was generated, the area of muscle was isolated manually by drawing a gate, a threshold was automatically applied using the Triangle setting, touching objects were split using the watershed function, and objects were counted using the analyze particles function cutting off objects smaller than 2 pixels. The number and area of lysosomes were measured using the

maximum intensity projection image, and the area of the drawn gate served as total tissue area. For object-based colocalization experiments (Fig. 5B-F), Keima was excited using 488 nm and 561 nm lasers using a microscope equipped with a 640 nm laser needed to excite LysoTracker Far Red (this microscope does not have a 440 nm laser). 488 nm exposure excites both acidic and neutral/basic mitochondria, whereas 561 nm excitation heavily favors excitation of acidic mitochondria. Thus, healthy mitochondria were segmented using an image generated using the following equation: (Keima488 channel) / (Keima561 channel + 1). One myotome was manually segmented, and all objects were counted within. Mitolysosomes were segmented using an image generated using the following equation (Keima561 channel) / (Keima488 channel + 150). EGFP-Lc3^{+} and LysoTracker Deep Red^{+} objects were segmented as described above. Object-based colocalization was performed using distance transformations from each object category, and objects near the edges of the somite or image border were excluded. Lc3^{+} objects were considered autolysosomes if there was a LysoTracker Deep Red object within 1 nm of it (filtered by Signal Intensity > 1 in the LysoTracker Deep Red objects distance transformation channel). If not, they were considered autophagosomes. An autophagosome or autolysosome was considered "in contact" with a healthy mitochondrion if there was a Keima488/561 object within 0 nm of it (filtered by Signal Intensity > 0 in the Keima488/561 objects distance transformation channel). A mitolysosome was considered near an Lc3^{+} object if it was within 0.5 μm (filtered by Signal Intensity > 500 in the Lc3^{+} objects distance transformation channel).

Morpholino Injections: Morpholinos (GeneTools, LLC) were reconstituted to 1 mM stock solutions in water. The injection mixes were prepared at 0.9 mM (*atg5*), 0.4 mM (*vhl*), or 0.2 mM (*pink1*), and 2 nL was injected into the yolk of 1-cell stage embryos. The sequences are listed in the Reagents and Resources Table.

CRISPR: All CRISPR genome editing was performed using a variation of the high-efficiency protocol described (Burger et al., 2016). Guide RNA sequences were designed using CHOPCHOP

(Labun et al., 2019) and chosen to target a 5' exonic region with the potential to introduce STOP codons in the event of frameshift. Alt-R crRNA (IDT) constructs were reconstituted and annealed with Alt-R tracrRNA (IDT) to form gRNA duplexes according to the manufacturer's instructions. Injection mixes were prepared by mixing 1 μL the gRNA duplex, 1 μL Duplex Buffer (IDT), and 1 μL ENGEN Spy Cas9 NLS (NEB) and allowing the mix to incubate at room temperature for at least 10 min. Approximately 2 nL of injection mix was injected into both the cell and yolk of 1-cell stage embryos. Efficient editing was confirmed by PCR and Sanger sequencing. For experiments using F0 CRISPR editing, the Sanger sequencing trace of each imaged larva was used to determine the extent of editing in a blinded manner. Editing was considered sufficient if trace files showed a mixture of multiple traces emerging near the PAM site. Images from larvae found to have low or no editing were removed from analysis (Figure 7—figure supplement 2).

Genotyping: DNA from individual larvae was extracted using proteinase K (Invitrogen) and amplified by PCR with the primer pairs (IDT) listed in the Key Resources Table. The 5' primer of the *pink1*^{gi2} PCR genotyping primer pair was synthesized with a 5' 6-FAM (Fluorescein) fluorescent dye attachment necessary for DNA Fragment Analysis, in which small, fluorescently-labeled DNA fragments are electrophoretically separated such that precise changes in size (down to 1 bp) can be detected. The *pink1*^{gi2} mutant fish (Zhang et al., 2017) were identified by a small deletion, which was detected using DNA Fragment Analysis (MGH CCIB DNA Core). Efficient editing in F0 high-efficiency CRISPR experiments was confirmed by Sanger sequencing, as described in the CRISPR section.

Statistical Analyses: All graphs and statistical analyses were generated using Prism (GraphPad). All bar graphs display the mean + SEM unless otherwise stated in the figure legend. For comparisons between only two conditions, standard, unpaired, two-tailed Student's t-tests were employed. For comparisons within groups with 4 conditions, two-way ANOVA with Holm-Sidak's multiple comparisons test were employed. *P* values or an asterisk indicating significant

differences as defined in the figure legends were included in each figure containing statistical analyses. Figure supplements were included for specific quantitative experiments to highlight reproducibility and full statistical analyses.

ACKNOWLEDGEMENTS

Research was supported by NIH F32AA025271 and the American Liver Foundation (P.J.W.), NIH R37 NS083524 to J.W.H., and NIH R01DK090311, R01DK105198, R24OD017870 to W.G.. W.G. is a Pew Scholar in the Biomedical Sciences. We thank Tom Schwarz for helpful discussions. We thank Nadine Budrow for maintaining our zebrafish colonies. We thank Phil Elks for sharing *DA-hif* plasmids, Donghun Shin for sharing the p5E-2.8fabp10a plasmid, and Daniel Hesselson for sharing the *pink1*^{gi2} line. We thank the Harvard Medical School MicRoN team for access to microscopes and imaging expertise.

AUTHOR CONTRIBUTIONS

Conceptualization, P.J.W., J-M.H., J.W.H., and W.G.; Methodology, P.J.W., A.S., and J-M.H.; Investigation, P.J.W., E.D.Q., and K.A.L.; Writing – Original Draft, P.J.W. and W.G.; Writing – Review and Editing, P.J.W., A.S., J-M.H., E.D.Q., J.W.H. and W.G.; Supervision, J.W.H. and W.G.; Funding Acquisition, P.J.W., J.W.H., and W.G.

DECLARATION OF INTERESTS

J.W.H. is a founder and consultant to Caraway Therapeutics and on an advisory board for X-Chem Inc. W.G. is a consultant to Camp4 Therapeutics and Amagma Therapeutics and receives royalties from FATE Therapeutics.

REFERENCES

Abeliovich H, Zarei M, Rigbolt KTG, Youle RJ, Dengjel J. 2013. Involvement of mitochondrial dynamics in the segregation of mitochondrial matrix proteins during stationary phase

mitophagy. *Nat Commun* **4**:2789.

Abudu YP, Pankiv S, Mathai BJ, Håkon Lystad A, Bindesbøll C, Brenne HB, Yoke Wui Ng M, Thiede B, Yamamoto A, Mutugi Nthiga T, Lamark T, Esguerra C V., Johansen T, Simonsen A. 2019. NIPSNAP1 and NIPSNAP2 Act as "Eat Me" Signals for Mitophagy. *Dev Cell* **49**:509-525.e12. doi:10.1016/j.devcel.2019.03.013

Anding AL, Baehrecke EH. 2017. Cleaning house: Selective autophagy of organelles. *Dev Cell* **41**:10–22. doi:10.1016/j.devcel.2017.02.016

Berger J, Currie PD. 2013. 503Unc, a Small and Muscle-Specific Zebrafish Promoter. *Genesis* **51**:443–447. doi:10.1002/dvg.22385

Bill BR, Petzold AM, Clark KJ, Schimmenti LA, Ekker SC. 2009. A primer for morpholino use in zebrafish. *Zebrafish* **6**:69–77. doi:10.1089/zeb.2008.0555

Birgisdottir A, Lamark T, Johansen T. 2013. The LIR motif – crucial for selective autophagy. *J Cell Sci* **126**:3237–3247.

Burger A, Lindsay H, Felker A, Hess C, Anders C, Chiavacci E, Zaugg J, Weber LM, Catena R, Jinek M, Robinson MD, Mosimann C. 2016. Maximizing mutagenesis with solubilized CRISPR-Cas9 ribonucleoprotein complexes. *Development* **143**:2025–2037. doi:10.1242/dev.134809

Burman JL, Pickles S, Wang C, Sekine S, Vargas JNS, Zhang Z, Youle AM, Nezich CL, Wu X, Hammer JA, Youle RJ. 2017. Mitochondrial fission facilitates the selective mitophagy of protein aggregates. *J Cell Biol* **216**:3231–3247. doi:10.1083/jcb.201612106

Cadete VJJ, Deschênes S, Cuillerier A, Brisebois F, Sugiura A, Vincent A, Turnbull D, Picard M, McBride HM, Burelle Y. 2016. Formation of mitochondrial-derived vesicles is an active and physiologically relevant mitochondrial quality control process in the cardiac system. *J*

Physiol **594**:5343–5362. doi:10.1113/JP272703

Chen G, Han Z, Feng D, Chen Y, Chen L, Wu H, Huang L, Zhou C, Cai X, Fu C, Duan L, Wang X, Liu L, Liu X, Shen Y, Zhu Y, Chen Q. 2014. A regulatory signaling loop comprising the PGAM5 phosphatase and CK2 controls receptor-mediated mitophagy. *Mol Cell* **54**:362–77.

Clark IE, Dodson MW, Jiang C, Cao JH, Huh JR, Seol JH, Yoo SJ, Hay BA, Guo M. 2006. Drosophila pink1 is required for mitochondrial function and interacts genetically with parkin. *Nature* **441**:1162–1166. doi:10.1038/nature04779

Cox AG, Goessling W. 2015. The lure of zebrafish in liver research: Regulation of hepatic growth in development and regeneration. *Curr Opin Genet Dev* **32**:153–161. doi:10.1016/j.gde.2015.03.002

Elks PM, Brizee S, van der Vaart M, Walmsley SR, van Eeden FJ, Renshaw SA, Meijer AH. 2013. Hypoxia Inducible Factor Signaling Modulates Susceptibility to Mycobacterial Infection via a Nitric Oxide Dependent Mechanism. *PLoS Pathog* **9**:e1003789. doi:10.1371/journal.ppat.1003789

Elks PM, Van Eeden FJ, Dixon G, Wang X, Reyes-Aldasoro CC, Ingham PW, Whyte MKB, Walmsley SR, Renshaw SA. 2011. Activation of hypoxia-inducible factor-1α (hif-1α) delays inflammation resolution by reducing neutrophil apoptosis and reverse migration in a zebrafish inflammation model. *Blood* **118**:712–722. doi:10.1182/blood-2010-12-324186

Evans CS, Holzbaur EL. 2020. Degradation of engulfed mitochondria is rate-limiting in Optineurin-mediated mitophagy in neurons. *Elife* **9**:e50260. doi:10.7554/eLife.50260

Ferdinand P, Roffe C. 2016. Hypoxia after stroke: A review of experimental and clinical evidence. *Exp Transl Stroke Med* **8**:1–8. doi:10.1186/s13231-016-0023-0

Friedman JR, Nunnari J. 2014. Mitochondrial form and function. *Nature* **505**:335–343.

doi:10.1038/nature12985

Gasser T. 2009. Mendelian forms of Parkinson's disease. *Biochim Biophys Acta - Mol Basis Dis* **1792**:587–596. doi:10.1016/j.bbadis.2008.12.007

Hamacher-Brady A, Brady NR, Logue SE, Sayen MR, Jinno M, Kirshenbaum LA, Gottlieb RA, Gustafsson ÅB. 2007. Response to myocardial ischemia/reperfusion injury involves Bnip3 and autophagy. *Cell Death Differ* **14**:146–157. doi:10.1038/sj.cdd.4401936

Harper JW, Ordureau A, Heo JM. 2018. Building and decoding ubiquitin chains for mitophagy. *Nat Rev Mol Cell Biol* **19**:93–108. doi:10.1038/nrm.2017.129

Harris JM, Esain V, Frechette GM, Harris LJ, Cox AG, Cortes M, Garnaas MK, Carroll KJ, Cutting CC, Khan T, Elks PM, Renshaw S a., Dickinson BC, Chang CJ, Murphy MP, Paw BH, Vander Heiden MG, Goessling W, North TE. 2013. Glucose metabolism impacts the spatiotemporal onset and magnitude of HSC induction in vivo. *Blood* **121**:2483–2493. doi:10.1182/blood-2012-12-471201

He C, Bartholomew CR, Zhou W, Klionsky DJ. 2009. Assaying autophagic activity in transgenic GFP-Lc3 and GFP-Gabarap zebrafish embryos. *Autophagy* **5**:520–526. doi:10.4161/auto.5.4.7768

Her GM, Chiang C-C, Chen W-Y, Wu J-L. 2003. In vivo studies of liver-type fatty acid binding protein (L-FABP) gene expression in liver of transgenic zebrafish (Danio rerio). *FEBS Lett* **538**:125–133. doi:10.1016/S0014-5793(03)00157-1

Iliopoulos O, Levy AP, Jiang C, Kaelin WG, Goldberg MA. 1996. Negative regulation of hypoxia-inducible genes by the von Hippel-Lindau protein. *Proc Natl Acad Sci* **93**:10595–10599. doi:10.1073/pnas.93.20.10595

Ivan M, Kondo K, Yang H, Kim W, Valiando J, Ohh M, Salic A, Asara JM, Lane WS, Kaelin J.

2001. HIFα targeted for VHL-mediated destruction by proline hydroxylation: Implications for O2 sensing. *Science* **292**:464–468. doi:10.1126/science.1059817

Kaelin WG, McKnight SL. 2013. Influence of metabolism on epigenetics and disease. *Cell* **153**:56–69. doi:10.1016/j.cell.2013.03.004

Katayama H, Hama H, Nagasawa K, Kurokawa H, Sugiyama M, Ando R, Funata M, Yoshida N, Homma M, Nishimura T, Takahashi M, Ishida Y, Hioki H, Tsujihata Y, Miyawaki A. 2020. Visualizing and Modulating Mitophagy for Therapeutic Studies of Neurodegeneration Resource Visualizing and Modulating Mitophagy for Therapeutic Studies of Neurodegeneration. *Cell* **181**:1–12. doi:10.1016/j.cell.2020.04.025

Katayama H, Kogure T, Mizushima N, Yoshimori T, Miyawaki A. 2011. A sensitive and quantitative technique for detecting autophagic events based on lysosomal delivery. *Chem Biol* **18**:1042–1052. doi:10.1016/j.chembiol.2011.05.013

Katayama H, Yamamoto A, Mizushima N, Yoshimori T, Miyawaki A. 2008. GFP-like proteins stably accumulate in lysosomes. *Cell Struct Funct* **33**:1–12. doi:10.1247/csf.07011

Kim YY, Um J, Yoon J, Kim H, Lee YJ, Jee HJ, Kim YM, Jang JS, Jang Y, Chung J, Park HT, Finkel T, Koh H, Yun J. 2019. Assessment of mitophagy in mt-Keima Drosophila revealed an essential role of the PINK1-Parkin pathway in mitophagy induction in vivo. *FASEB J* **33**:9742–9751. doi:10.1096/fj.201900073R

Kolitsida P, Zhou J, Rackiewicz M, Nolic V, Dengjel J, Abeliovich H. 2019. Phosphorylation of mitochondrial matrix proteins regulates their selective mitophagic degradation. *Proc Natl Acad Sci* **116**:20517–20527. doi:10.1073/pnas.1901759116

Kwan KM, Fujimoto E, Grabher C, Mangum BD, Hardy ME, Campbell DS, Parant JM, Yost HJ, Kanki JP, Chien C Bin. 2007. The Tol2kit: A multisite gateway-based construction Kit for Tol2 transposon transgenesis constructs. *Dev Dyn* **236**:3088–3099.

doi:10.1002/dvdy.21343

Labun K, Montague TG, Krause M, Torres Cleuren YN, Tjeldnes H, Valen E. 2019. CHOPCHOP v3: expanding the CRISPR web toolbox beyond genome editing. *Nucleic Acids Res* **47**:W171–W174. doi:10.1093/nar/gkz365

Le Guerroué F, Eck F, Jung J, Starzetz T, Mittelbronn M, Kaulich M, Behrends C. 2017. Autophagosomal Content Profiling Reveals an LC3C-Dependent Piecemeal Mitophagy Pathway. *Mol Cell* **68**:786-796.e6. doi:10.1016/j.molcel.2017.10.029

Lee E, Koo Y, Ng A, Wei Y, Luby-Phelps K, Juraszek A, Xavier RJ, Cleaver O, Levine B, Amatruda JF. 2014. Autophagy is essential for cardiac morphogenesis during vertebrate development. *Autophagy* **10**:572–587. doi:10.4161/auto.27649

Lee E, Wei Y, Zou Z, Tucker K, Rakheja D, Levine B, Amatruda JF. 2016. Genetic inhibition of autophagy promotes p53 loss-of-heterozygosity and tumorigenesis. *Oncotarget* **7**. doi:10.18632/oncotarget.12084

Lee JJ, Sanchez-Martinez A, Zarate AM, Benincá C, Mayor U, Clague MJ, Whitworth AJ. 2018. Basal mitophagy is widespread in Drosophila but minimally affected by loss of Pink1 or parkin. *J Cell Biol* **217**:1613–1622. doi:10.1083/jcb.201801044

Lee JW, Ko J, Ju C, Eltzschig HK. 2019. Hypoxia signaling in human diseases and therapeutic targets. *Exp Mol Med* **51**:1–13. doi:10.1038/s12276-019-0235-1

Leermakers PA, Gosker HR. 2016. Skeletal muscle mitophagy in chronic disease: Implications for muscle oxidative capacity. *Curr Opin Clin Nutr Metab Care* **19**:427–433. doi:10.1097/MCO.0000000000000319

Liu L, Feng D, Chen G, Chen M, Zheng Q, Song P, Ma Q, Zhu C, Wang R, Qi W, Huang L, Xue P, Li B, Wang X, Jin H, Wang J, Yang F, Liu P, Zhu Y, Sui S, Chen Q. 2012. Mitochondrial

outer-membrane protein FUNDC1 mediates hypoxia-induced mitophagy in mammalian cells. *Nat Cell Biol* **14**:177–185. doi:10.1038/ncb2422

Mammucari C, Milan G, Romanello V, Masiero E, Rudolf R, Del Piccolo P, Burden SJ, Di Lisi R, Sandri C, Zhao J, Goldberg AL, Schiaffino S, Sandri M. 2007. FoxO3 Controls Autophagy in Skeletal Muscle In Vivo. *Cell Metab* **6**:458–471. doi:10.1016/j.cmet.2007.11.001

Mao K, Wang K, Zhao M, Xu T, Klionsky DJ. 2011. Two MAPK-signaling pathways are required for mitophagy in Saccharomyces cerevisiae. *J Cell Biol* **193**:755–767. doi:10.1083/jcb.201102092

McWilliams TG, Prescott AR, Allen GFG, Tamjar J, Munson MJ, Thomson C, Muqit MMK, Ganley IG. 2016. Mito-QC illuminates mitophagy and mitochondrial architecture in vivo. *J Cell Biol* **214**:333–345. doi:10.1083/jcb.201603039

McWilliams TG, Prescott AR, Montava-Garriga L, Ball G, Singh F, Barini E, Muqit MMK, Brooks SP, Ganley IG. 2018. Basal Mitophagy Occurs Independently of PINK1 in Mouse Tissues of High Metabolic Demand. *Cell Metab* **27**:439-449.e5. doi:10.1016/j.cmet.2017.12.008

Mosimann C, Kaufman CK, Li P, Pugach EK, Tamplin OJ, Zon LI. 2011. Ubiquitous transgene expression and Cre-based recombination driven by the ubiquitin promoter in zebrafish. *Development* **138**:169–177. doi:10.1242/dev.059345

Mosimann C, Zon LI. 2011. Advanced zebrafish transgenesis with Tol2 and application for Cre/lox recombination experiments. *Methods Cell Biol* **104**:173–194. doi:10.1016/B978-0-12-374814-0.00010-0

Ordureau A, Paulo JA, Zhang J, An H, Swatek KN, Cannon JR, Wan Q, Komander D, Harper JW. 2020. Global Landscape and Dynamics of Parkin and USP30-Dependent Ubiquitylomes in iNeurons during Mitophagic Signaling. *Mol Cell* **77**:1124-1142.e10. doi:10.1016/j.molcel.2019.11.013

Park J, Lee SB, Lee S, Kim Y, Song S, Kim S, Bae E, Kim J, Shong M, Kim JM, Chung J. 2006. Mitochondrial dysfunction in Drosophila PINK1 mutants is complemented by parkin. *Nature* **441**:1157–1161. doi:10.1038/nature04788

Pickles S, Vigié P, Youle RJ. 2018. Mitophagy and Quality Control Mechanisms in Mitochondrial Maintenance. *Curr Biol* **28**:R170–R185. doi:10.1016/j.cub.2018.01.004

Pickrell AM, Youle RJ. 2015. The roles of PINK1, Parkin, and mitochondrial fidelity in parkinson's disease. *Neuron* **85**:257–273. doi:10.1016/j.neuron.2014.12.007

Porcelli AM, Ghelli A, Zanna C, Pinton P, Rizzuto R, Rugolo M. 2005. pH difference across the outer mitochondrial membrane measured with a green fluorescent protein mutant. *Biochem Biophys Res Commun* **326**:799–804. doi:10.1016/j.bbrc.2004.11.105

Preidis GA, Kim KH, Moore DD. 2017. Nutrient-sensing nuclear receptors PPAR? and FXR control liver energy balance. *J Clin Invest* **127**:1193–1201. doi:10.1172/JCI88893

Priyadarshini M, Tuimala J, Chen YC, Panula P. 2013. A zebrafish model of PINK1 deficiency reveals key pathway dysfunction including HIF signaling. *Neurobiol Dis* **54**:127–138. doi:10.1016/j.nbd.2013.02.002

Raefsky SM, Mattson MP. 2017. Adaptive responses of neuronal mitochondria to bioenergetic challenges: Roles in neuroplasticity and disease resistance. *Free Radic Biol Med* **102**:203–216. doi:10.1016/j.freeradbiomed.2016.11.045

Rodger CE, Mcwilliams TG, Ganley Ian G, Ganley I G. 2018. Mammalian mitophagy – from in vitro molecules to in vivo models. *FEBS J* **285**:1185–1202.

Rodríguez-Nuevo A, Díaz-Ramos A, Noguera E, Díaz-Sáez F, Duran X, Muñoz JP, Romero M, Plana N, Sebastián D, Tezze C, Romanello V, Ribas F, Seco J, Planet E, Doctrow SR, González J, Borràs M, Liesa M, Palacín M, Vendrell J, Villarroya F, Sandri M, Shirihai O,

Zorzano A. 2018. Mitochondrial DNA and TLR9 drive muscle inflammation upon Opa1 deficiency. *EMBO J* **37**:1–18. doi:10.15252/embj.201796553

Rojansky R, Cha MY, Chan DC. 2016. Elimination of paternal mitochondria in mouse embryos occurs through autophagic degradation dependent on PARKIN and MUL1. *Elife* **5**:e17896. doi:10.7554/eLife.17896

Romanello V, Sandri M. 2013. Mitochondrial biogenesis and fragmentation as regulators of protein degradation in striated muscles. *J Mol Cell Cardiol* **55**:64–72. doi:10.1016/j.yjmcc.2012.08.001

Ronan B, Flamand O, Vescovi L, Dureuil C, Durand L, Fassy F, Bachelot MF, Lamberton A, Mathieu M, Bertrand T, Marquette JP, El-Ahmad Y, Filoche-Romme B, Schio L, Garcia-Echeverria C, Goulaouic H, Pasquier B. 2014. A highly potent and selective Vps34 inhibitor alters vesicle trafficking and autophagy. *Nat Chem Biol* **10**:1013–1019. doi:10.1038/nchembio.1681

Sandri M. 2013. Protein breakdown in muscle wasting: Role of autophagy-lysosome and ubiquitin-proteasome. *Int J Biochem Cell Biol* **45**:2121–2129. doi:10.1016/j.biocel.2013.04.023

Sebastián D, Zorzano A. 2020. Self-Eating for Muscle Fitness: Autophagy in the Control of Energy Metabolism. *Dev Cell* **54**:268–281. doi:10.1016/j.devcel.2020.06.030

Settembre C, Fraldi A, Medina DL, Ballabio A. 2013. Signals from the lysosome: A control centre for cellular clearance and energy metabolism. *Nat Rev Mol Cell Biol* **14**:283–296. doi:10.1038/nrm3565

Shi RY, Zhu SH, Li V, Gibson SB, Xu XS, Kong JM. 2014. BNIP3 interacting with LC3 triggers excessive mitophagy in delayed neuronal death in stroke. *CNS Neurosci Ther* **20**:1045–1055. doi:10.1111/cns.12325

Smirnova E, Shurland DL, Ryazantsev SN, Van Der Bliek AM. 1998. A human dynamin-related protein controls the distribution of mitochondria. *J Cell Biol* **143**:351–358. doi:10.1083/jcb.143.2.351

Sugiura A, McLelland G, Fon EA, McBride HM. 2014. A new pathway for mitochondrial quality control: mitochondrial-derived vesicles. *EMBO J* **33**:2142–2156. doi:10.15252/embj.201488104

Sun N, Yun J, Liu J, Malide D, Liu C, Rovira II, Holmström KM, Fergusson MM, Yoo YH, Combs CA, Finkel T. 2015. Measuring In Vivo Mitophagy. *Mol Cell* **60**:685–696. doi:10.1016/j.molcel.2015.10.009

Vargas JNS, Wang C, Bunker E, Hao L, Maric D, Schiavo G, Randow F, Youle RJ. 2019. Spatiotemporal Control of ULK1 Activation by NDP52 and TBK1 during Selective Autophagy. *Mol Cell* **74**:347-362.e6. doi:10.1016/j.molcel.2019.02.010

Wilson C. 2012. Aspects of larval rearing. *ILAR J* **53**:169–178. doi:10.1093/ilar.53.2.169

Wrighton PJ, Oderberg IM, Goessling W. 2019. There Is Something Fishy About Liver Cancer: Zebrafish Models of Hepatocellular Carcinoma. *Cell Mol Gastroenterol Hepatol* **8**:347–363. doi:10.1016/j.jcmgh.2019.05.002

Yamashita SI, Jin X, Furukawa K, Hamasaki M, Nezu A, Otera H, Saigusa T, Yoshimori T, Sakai Y, Mihara K, Kanki T. 2016. Mitochondrial division occurs concurrently with autophagosome formation but independently of Drp1 during mitophagy. *J Cell Biol* **215**:649–665. doi:10.1083/jcb.201605093

Yang W, Liu Y, Tu Z, Xiao C, Yan S, Ma X, Guo X, Chen X, Yin P, Yang Z, Yang S, Jiang T, Li S, Qin C, Li XJ. 2019. CRISPR/Cas9-mediated PINK1 deletion leads to neurodegeneration in rhesus monkeys. *Cell Res* **29**:334–336. doi:10.1038/s41422-019-0142-y

Yang Y, Gehrke S, Imai Y, Huang Z, Ouyang Y, Wang JW, Yang L, Beal MF, Vogel H, Lu B. 2006. Mitochondrial pathology and muscle and dopaminergic neuron degeneration caused by inactivation of Drosophila Pink1 is rescued by Parkin. *Proc Natl Acad Sci* **103**:10793–10798. doi:10.1073/pnas.0602493103

Yoo S-M, Jung Y-K. 2018. A Molecular Approach to Mitophagy and Mitochondrial Dynamics. *Mol Cells* **41**:18–26. doi:10.14348/molcells.2018.2277

Youle RJ. 2019. Mitochondria—Striking a balance between host and endosymbiont. *Science* **365**.

Yuan Y, Zheng Y, Zhang X, Chen Y, Wu X, Wu J, Shen Z, Jiang L, Wang L, Yang W, Luo J, Qin Z, Hu W, Chen Z. 2017. BNIP3L/NIX-mediated mitophagy protects against ischemic brain injury independent of PARK2. *Autophagy* **13**:1754–1766. doi:10.1080/15548627.2017.1357792

Zhang H, Bosch-Marce M, Shimoda LA, Yee ST, Jin HB, Wesley JB, Gonzalez FJ, Semenza GL. 2008. Mitochondrial autophagy is an HIF-1-dependent adaptive metabolic response to hypoxia. *J Biol Chem* **283**:10892–10903. doi:10.1074/jbc.M800102200

Zhang T, Xue L, Li L, Tang C, Wan Z, Wang R, Tan J, Tan Y, Han H, Tian R, Billiar TR, Tao WA, Zhang Z. 2016. BNIP3 protein suppresses PINK1 kinase proteolytic cleavage to promote mitophagy. *J Biol Chem* **291**:21616–21629. doi:10.1074/jbc.M116.733410

Zhang W, Ren H, Xu C, Zhu C, Wu H, Liu D, Wang J, Liu L, Li W, Ma Q, Du L, Zheng M, Zhang C, Liu J, Chen Q. 2016. Hypoxic mitophagy regulates mitochondrial quality and platelet activation and determines severity of I/R heart injury. *Elife* **5**:e21407.

Zhang Y, Nguyen DT, Olzomer EM, Poon GP, Cole NJ, Puvanendran A, Phillips BR, Hesselson D. 2017. Rescue of Pink1 Deficiency by Stress-Dependent Activation of Autophagy. *Cell Chem Biol* **24**:471-480.e4. doi:10.1016/j.chembiol.2017.03.005

Zhou H, Zhu P, Guo J, Hu N, Wang S, Li D, Hu S, Ren J, Cao F, Chen Y. 2017. Ripk3 induces mitochondrial apoptosis via inhibition of FUNDC1 mitophagy in cardiac IR injury. *Redox Biol* **13**:498–507.

Zhou Y, Long Q, Wu H, Li W, Qi J, Wu Y, Xiang G, Tang H, Yang L, Chen K, Li L, Bao F, Li H, Wang Y, Li M, Liu X. 2019. Topology-dependent, bifurcated mitochondrial quality control under starvation. *Autophagy* **Jul**:1–13.